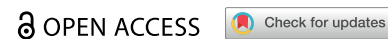



RESEARCH ARTICLE



Novel hybrids of 1,2,3-triazole-benzoxazole: design, synthesis, and assessment of DprE1 enzyme inhibitors using fluorometric assay and computational analysis

Manisha Singh^a, Sarah M. Batt^b, Christian S. C. Canales^c, Fernando R. Pavan^c, Sethu Arun Kumar^a, Handattu S. Akshatha^a, Meduri Bhagyalalitha^a, Karthik G. Pujar^a, Durgesh Bidye^a, Gurubasavaraj V. Pujar^a and Gurdial S. Besra^b 

^aComputer Aided Drug Design Lab, Department of Pharmaceutical Chemistry, JSS College of Pharmacy, JSS Academy of Higher Education and Research, Sri Shivarathreeswara Nagara, Mysore, India; ^bSchool of Biosciences, University of Birmingham, Birmingham, United Kingdom; ^cFaculty of Pharmaceutical Sciences, Paulista State University—UNESP, Araraquara, SP, Brazil

ABSTRACT

Decaprenylphosphoryl-β-D-ribose-oxidase (DprE1), a subunit of the essential decaprenylphosphoribose-2'-epimerase, plays a crucial role in the synthesis of cell wall arabinan components in mycobacteria, including the pathogen responsible for tuberculosis, *Mycobacterium tuberculosis*. In this study, we designed, synthesised, and evaluated 15 (BOK-1–BOK-10 and BOP-1–BOP-5) potential inhibitors of DprE1 from a series of 1,2,3-triazole ligands using a validated DprE1 inhibition assay. Two compounds, BOK-2 and BOK-3, demonstrated significant inhibition with IC₅₀ values of 2.2±0.1 and 3.0±0.6 μM, respectively, whereas the standard drug (TCA-1) showed inhibition at 3.0±0.2 μM. Through molecular modelling and dynamic simulations, we explored the structural relationships between selected 1,2,3-triazole compounds and DprE1, revealing key features for effective drug–target interactions. This study introduces a novel approach for designing ligands against DprE1, offering a potential therapeutic strategy for tuberculosis treatment.

HIGHLIGHTS



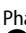
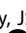
- Identification of 15 (BOK-1–BOK-10 and BOP-1–BOP-5) potent inhibitors of DprE1 enzyme from 1,2,3-triazole ligands.
- BOK-2 and BOK-3 exhibited significant DprE1 inhibition with IC₅₀ values of 2.2±0.1 and 3.0±0.6 μM, respectively.
- Molecular modelling and dynamic simulations elucidated key structural features for effective drug–target interactions.
- Novel approach introduced for designing DprE1 ligands, potentially aiding tuberculosis treatment.
- Findings offer promising candidates for future tuberculosis research.


ARTICLE HISTORY

Received 14 June 2024
Revised 16 August 2024
Accepted 6 September 2024

KEYWORDS

Tuberculosis; 1,2,3-triazoles;
DprE1 inhibitor assay

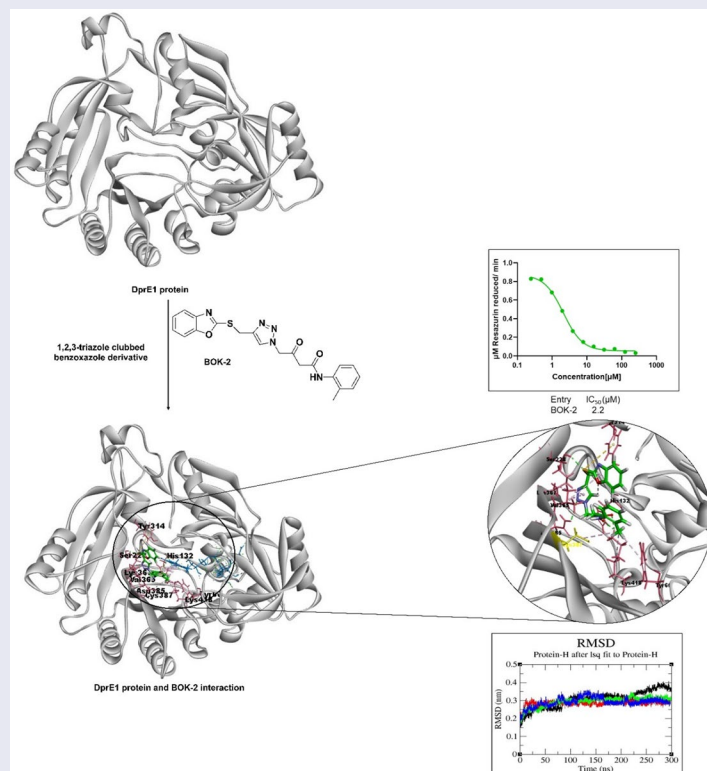
CONTACT Gurubasavaraj V. Pujar  gvpujar@jssuni.edu.in  Computer Aided Drug Design Lab, Department of Pharmaceutical Chemistry, JSS College of Pharmacy, JSS Academy of Higher Education and Research, Sri Shivarathreeswara Nagara, Mysore, India; Gurdial S. Besra  g.besra@bham.ac.uk  School of Biosciences, University of Birmingham, Birmingham, United Kingdom

 Supplemental data for this article can be accessed online at <https://doi.org/10.1080/14756366.2024.2403744>.

© 2024 The Author(s). Published by Informa UK Limited, trading as Taylor & Francis Group.

This is an Open Access article distributed under the terms of the Creative Commons Attribution License (<http://creativecommons.org/licenses/by/4.0/>), which permits unrestricted use, distribution, and reproduction in any medium, provided the original work is properly cited. The terms on which this article has been published allow the posting of the Accepted Manuscript in a repository by the author(s) or with their consent.

GRAPHICAL ABSTRACT



Introduction

Tuberculosis (TB) continues to be a significant global health issue, with the emergence of drug-resistant TB (DR-TB) presenting a considerable challenge¹. The increasing prevalence of DR-TB can complicate TB treatment, leading to higher failure rates, extended therapy durations, and more complex medication regimens^{1,2}. Currently, TB treatment involves different therapeutic approaches, which can increase to 2 years for DR-TB. This lengthy treatment, along with the associated side effects, often results in patients prematurely discontinuing their treatment, exacerbating the issue of drug resistance². Furthermore, the effect of the Coronavirus Disease - 2019 (COVID-19) pandemic has the potential to disrupt the prompt identification and treatment of newly diagnosed TB cases, adding to the burden of TB³.

In the fight against TB, a major obstacle is the limited availability of newer and more effective drugs. Since rifampicin gained approval in the 1960s, the FDA has sanctioned only two additional anti-TB drugs, namely pretomanid and bedaquiline⁴. Despite ongoing efforts, there is a pressing need to discover and develop newer and more efficacious anti-TB drugs. Among many approaches, treating tuberculosis could be achieved by inhibiting the mycobacterium cell wall synthesis⁵. Primary drugs like ethambutol and isoniazid inhibit key enzymes of *Mycobacterium tuberculosis* (Mtb) involved in the synthesis of the arabinogalactan and mycolic acid layers, which are essential to protect the cell from antibiotics and the host's defences⁶. Recent advancements in whole-cell screening have led to the discovery of new drug families that specifically interact with crucial target proteins involved in the formation of structural elements of the cell wall^{6,7}.

Decaprenylphosphoryl-β-D-ribose-oxidase (DprE1) is one such essential enzyme, catalysing the flavin adenine dinucleotide (FAD)-dependent oxidation of decaprenylphosphoryl-β-D-ribose (DPR) to produce decaprenyl phosphoryl-2'-keto-D-erythro-pentofuranose (DPX). The keto group of DPX subsequently undergoes a reduction by decaprenylphosphoryl-D-2-ketoerythropentose reductase (DprE2), resulting in the formation of decaprenylphosphoryl-β-D-arabinofuranose. This molecule serves as a vital lipid-linked substrate used by membrane bound arabinosyltransferases to construct the essential arabinan layers of the cell wall (Figure 1a)^{8,9}. The specificity of DprE1 for mycobacteria and actinomycetes makes it an enticing target for tuberculosis treatment development^{10,11}.

Numerous compounds that function as inhibitors of DprE1, through non-covalent interactions, have been discovered (Figure 1b). One noteworthy example is TCA-1, a benzothiazole derivative that distinguishes itself for its ability to inhibit both proliferating and non-proliferating forms of Mtb^{12,13}. The distinctive moiety in TCA-1, specifically the thiophene amide, has led us to shift our focus towards the discovery of a new series of 1,2,3-triazole clubbed benzoxazole derivatives, aiming for substantial improvement in TB drug discovery¹⁴. The goal is to improve their effectiveness and drug-like properties through the implementation of a scaffold-hopping strategy (Figure 1c), expanding on the foundation provided by the lead compound TCA-1¹⁵.

In the past 20 years, 1,2,3-triazoles have gained prominence as a crucial component in the field of drug development and discovery. This is predominantly attributed to their noteworthy biological efficacy, facile synthesis, stability across diverse conditions, and adaptability to a broad spectrum of chemical reactions¹⁶. The revolutionary concept, recognised with a Nobel Prize and originating from the Meldal and

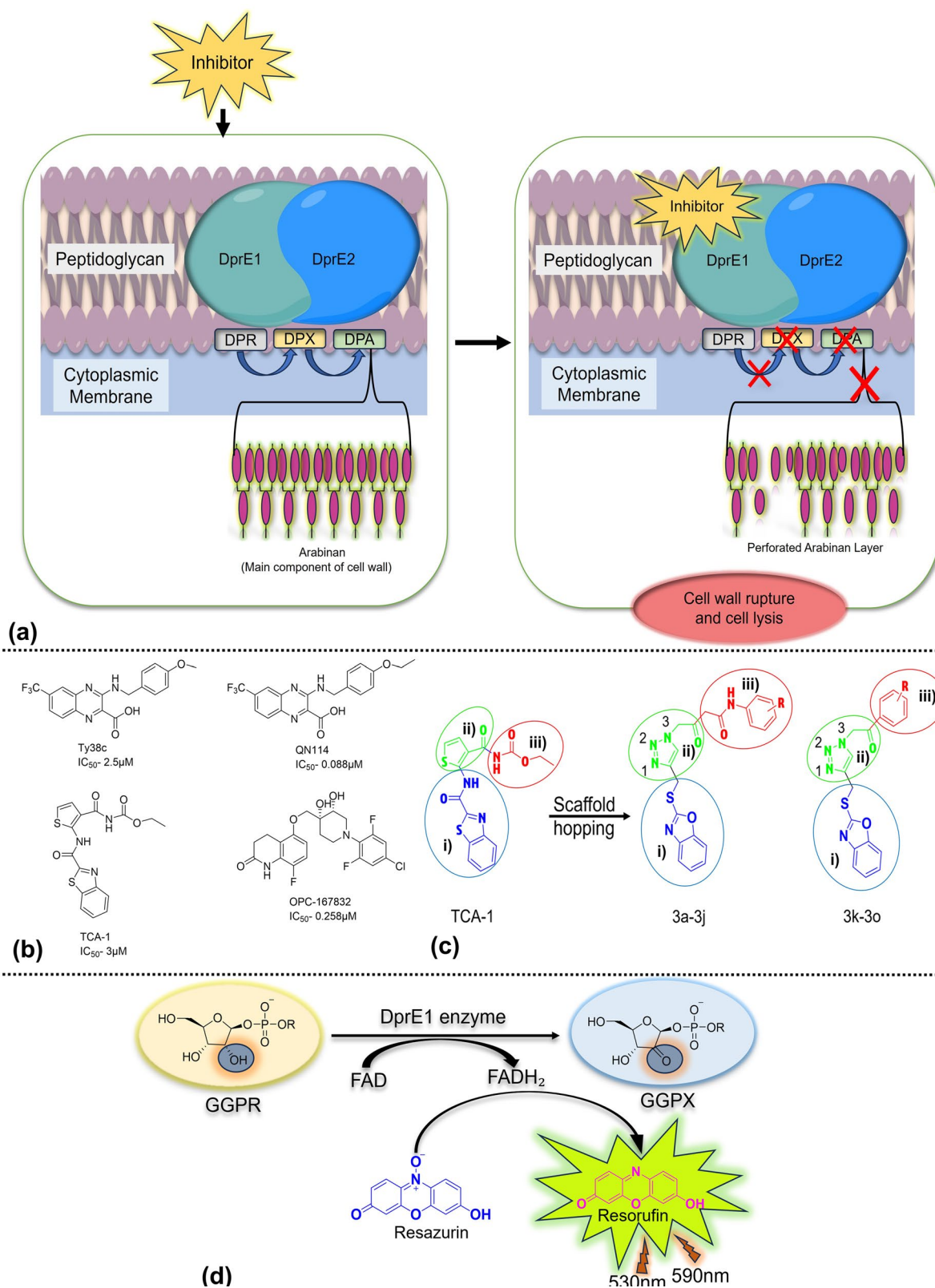


Figure 1. (a) DprE1 in the biosynthesis of arabinan in the cell wall of *Mtb* and the presence of inhibitor leading to interruption in arabinan biosynthesis. (b) Novel drug candidates: non-covalent inhibitors of DprE1 demonstrating IC_{50} values at early stages. (c) Scaffold-hopping strategy: polar tail (in circle iii), hydrophobic head (in circle ii), and lipophilic trunk (in circle i). Exploration of novel ligands through the chemical structures of DprE1 inhibitor (TCA-1). (d) The DprE1 assay measures DprE1 activity using a fluorescence-based assay that involves the reduction of resazurin to resorufin, while DprE1 catalyses the oxidation of GGPR to GGPX using FAD as the cofactor.

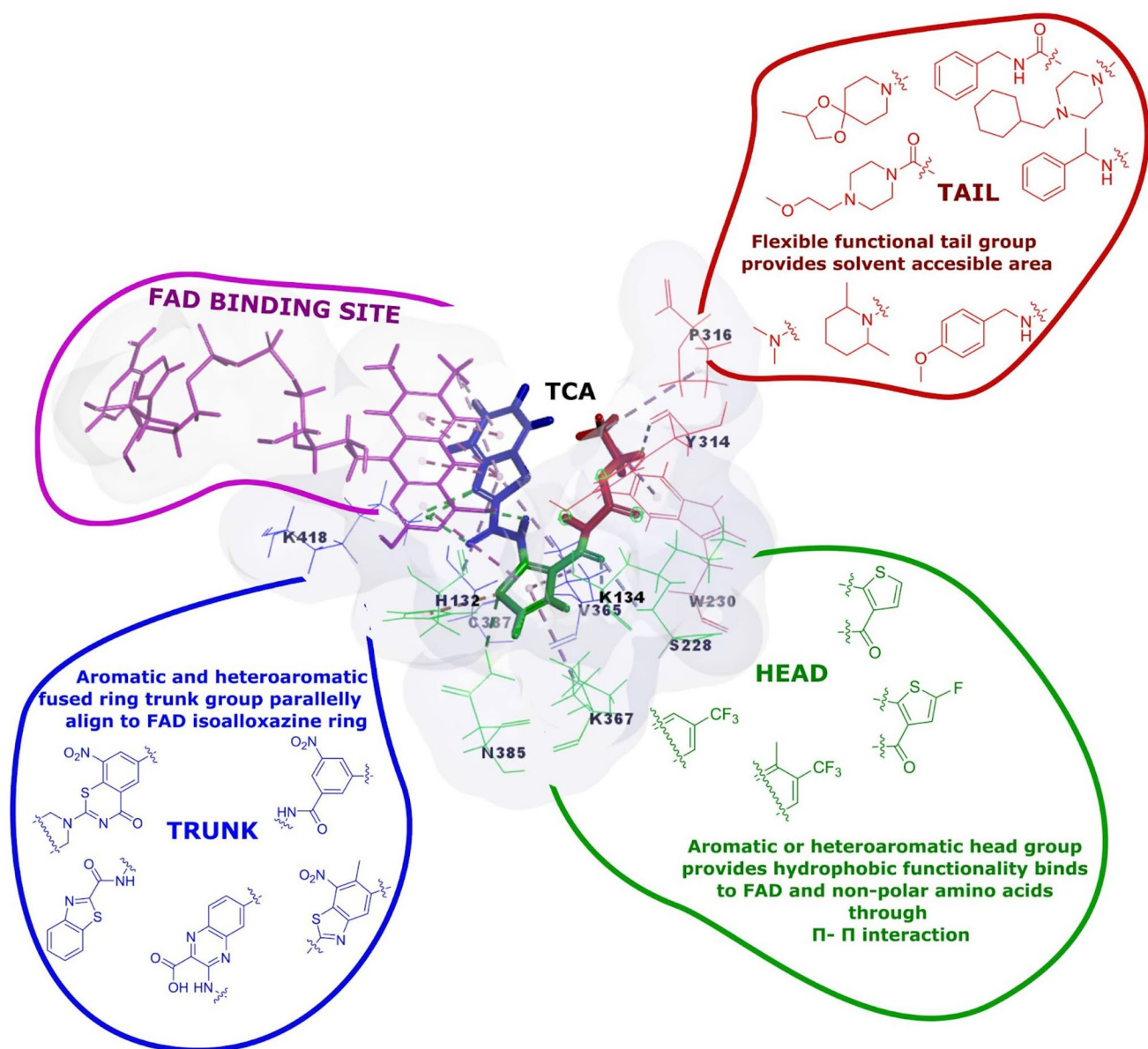


Figure 2. Visualisation of DprE1 enzyme's functional sites using the TCA-1 inhibitor: mapping polar tail area, hydrophobic head regions, and lipophilic trunk regions. The lipophilic region aligns with FAD's tricyclic hetero ring. (Inspired by Yadav et al.¹⁰).

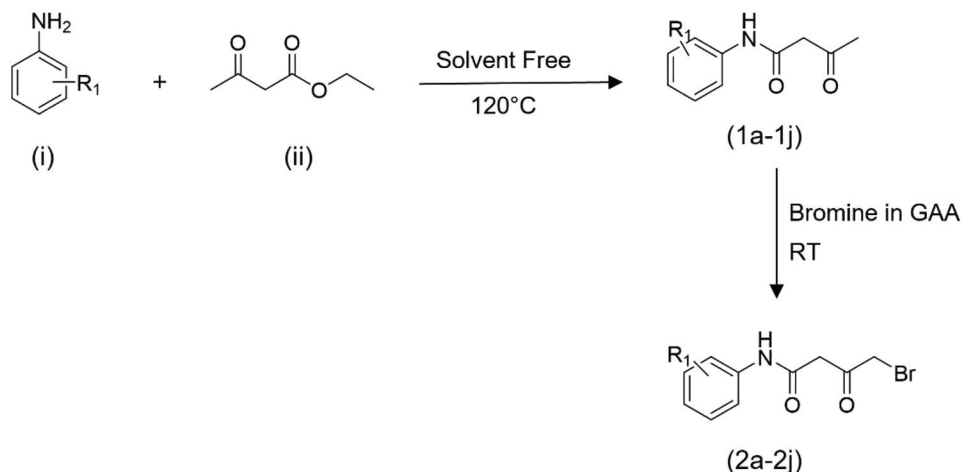
Sharpless groups, centred on refining the Huisgen 1,3-dipolar cycloaddition involving azides and terminal alkynes. This modification resulted in the production of 1,4-disubstituted 1,2,3-triazoles^{14,16}. 1,2,3-Triazole and benzoxazole-based molecules have diverse biological activities, such as antimicrobial, anti-cancer, and anti-tuberculosis effects^{17,18}. Acetoacetanilide, another intriguing pharmacophore, offers antimicrobial, antioxidant, and antiproliferative properties¹⁹. These scaffolds have potential for drug discovery, as proven with drugs such as rufinamide and benoxaprofen.

In the present work, we utilised molecular hybridisation that combines bioactive scaffolds to design and synthesise novel 1,2,3-triazole-linked benzoxazole derivatives to explore their anti-tubercular activity, addressing a gap in the previously reported *in-vitro* activity on DprE1 inhibition, which is guided by structure-activity relationships²⁰. A biochemical assay elucidated their mechanism of action and affinity towards DprE1 (Figure 1d), emphasising molecular design encompassing synthesis, redox assays, ADMET studies, molecular interaction, and dynamics simulation analyses.

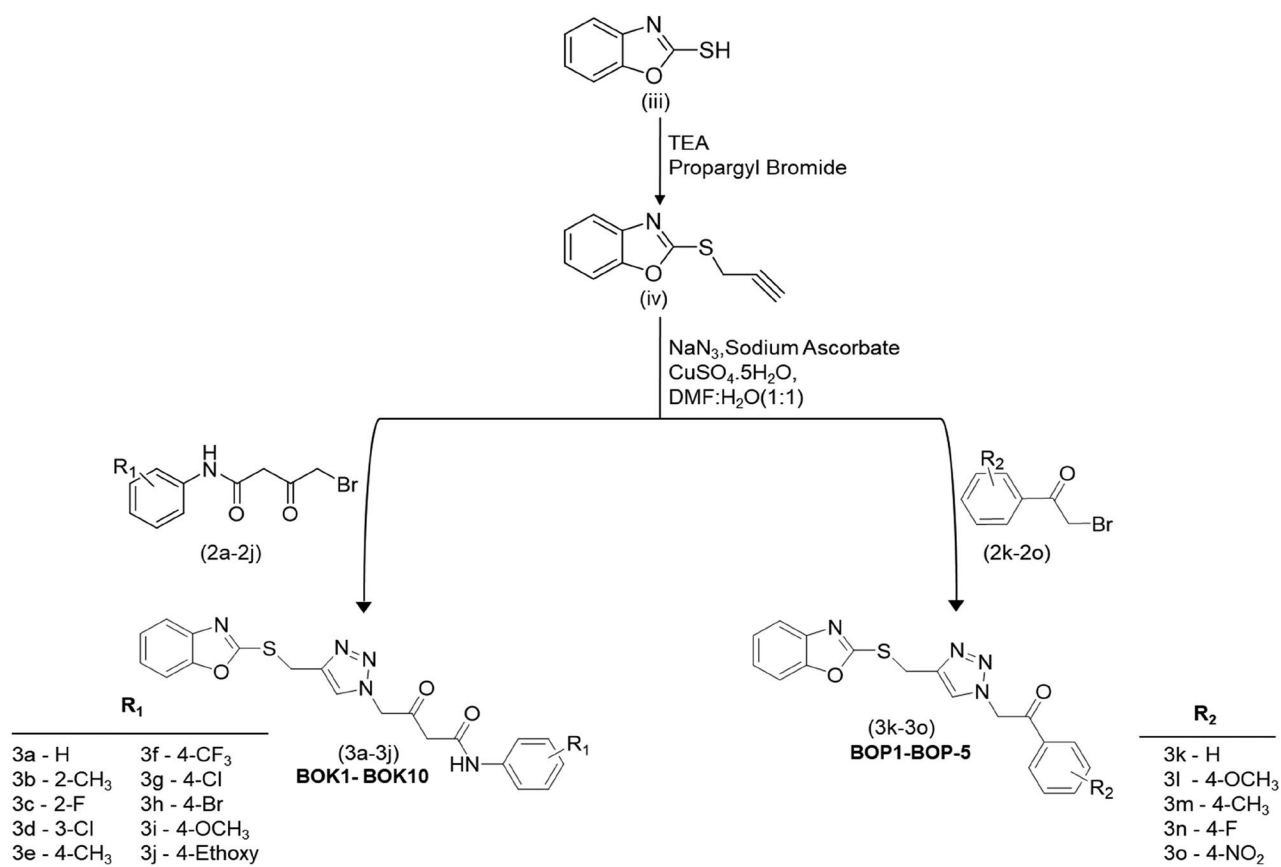
Results and discussion

Deciphering unique interaction of TCA-1 with DprE1

TCA-1, the reported DprE1 inhibitor, has a unique structure of thiophenamide molecule attached to benzothiazole moiety. Driven by the structural interplay and inhibition of DprE1 by the TCA-1 molecule, we sought to study the structure of TCA-1 and its interaction with the protein. The active-site pocket of DprE1 (Figure 2) includes distinct regions: a polar region containing Lys418, His132, and Ser228; a hydrophobic site with Cys387 and Gln334; and a lipophilic area featuring Asn324, Arg325, and Leu317. We identified these regions using Discovery Studio 19.0 software with the PDB ID 4KW5 where the co-crystal ligand is TCA-1. The confirmation of these findings was obtained through the DprE1 protein binding sheet, accessible in the Supporting Information section (see Fig.S46) on the PDBsum server. With this insight, we developed the rationale for designing structures with molecular requirements i.e. having a hydrophobic head (1,2,3-triazole ring), lipophilic



Scheme 1. Synthesis pathway for the ω -bromoacetoacetanilides.



Scheme 2. Novel synthesis of 1,2,3-triazole-linked benzoxazole phenacyl/acetoacetanilide derivatives.

trunk (benzoxazole ring), and polar tail (phenacyl/acetoacetanilide) that would align and complement with DprE1 protein, aiming to elicit desired biological responses.

Chemistry and synthesis

The synthesis of the titled compounds involved refluxing commercially available substituted anilines (i) with ethyl acetoacetate (ii) in a solvent-free condition for 2 h at 120°C, yielding substituted acetoacetanilides (1a–1j) as outlined in Scheme 1. Subsequently, the

intermediates (1a–1j) underwent bromination by employing a solution of bromine in glacial acetic acid, supplemented with a small crystal of iodine²¹. The reaction solution was stirred for 6–8 h at ambient temperature, leading to the formation of ω -bromoacetoacetanilides (2a–2j). Phenacyl bromide (2k–2o) was directly procured for use in Scheme 2. The synthesis of thiopropargylated benzoxazole (iv) was initiated with the utilisation of 2-mercapto benzoxazole (iii) as the substrate and propargyl bromide (80% in toluene). Propargylation occurred at the thiol group located at position 2 of benzoxazole through reflux conditions in absolute ethanol

with triethylamine as a basic catalyst, yielding the desired product in a high yield of 95% after 1 h. Subsequently, the final compounds (3a–3j or **BOK-1–BOK-10**) and (3k–3o or **BOP-1–BOP-5**) were generated through an azide–alkyne Huisgen cycloaddition reaction. In this process, thiopropargylated benzoxazole was combined with sodium azide, sodium ascorbate, and copper sulphate pentahydrate, along with either substituted ω -bromoacetoacetanilides or substituted phenacyl bromides. This reaction took place in a mixture of dimethylformamide (DMF) and H₂O (5:5) at ambient temperature. After stirring for 8–12 h, the final compounds were obtained in high yields, ranging from 80% to 95%. This method served as a versatile, one-pot, multicomponent reaction for the synthesis of these compounds, as illustrated in Scheme 2.

In the infra-red (IR) spectra, the presence of signals at $\sim 1707.06\text{ cm}^{-1}$ and $\sim 1666.55\text{ cm}^{-1}$ confirms the C=O and C=O stretching vibrations, respectively, indicating the formation of ω -bromoacetoacetanilide (1a–1j). This is further supported by a distinctive NH stretching signal at $\sim 3296.45\text{ cm}^{-1}$. Moreover, the integration of the propargyl residue at the thiol group at position 2 of the benzoxazole ring (iv) is confirmed by the presence of two clear bands appearing at approximately 3391 cm^{-1} and 2141 cm^{-1} , indicating the existence of the ethyne hydrogen ($\equiv\text{C-H}$) and the ethyne ($\text{C}\equiv\text{C}$) group, respectively.

The synthesis of compounds 3a–3j and 3k–3o was achieved through the absence of peaks corresponding to $\text{C}\equiv\text{C}$ at approximately 2141 cm^{-1} and $\equiv\text{C-H}$ at around 3391 cm^{-1} in the IR spectra confirming their participation in the cycloaddition reaction. Additionally, proton NMR analysis of the final compounds revealed the absence of signal assigned for the ethyne proton at $\delta\text{H} \sim 3.25\text{ ppm}$ in the starting 5-alkyne, along with the emergence of a singlet at $\delta\text{H} \sim 8.85\text{ ppm}$, indicative of $-\text{CH}$ proton of the 1,2,3-triazole, further confirming the successful formation of these compounds.

Assessment of minimal inhibitory concentration against the H37Rv strain of Mycobacterium tuberculosis

The compounds under investigation were assessed for their effectiveness in inhibiting the *in-vitro* growth of the *M. tuberculosis* H37Rv strain using the resazurin microtiter assay (REMA). Resazurin, employed as a redox indicator, exhibits a colorimetric transformation in correlation with the growth of *M. tuberculosis*. This alteration in colour was quantitatively assessed to gauge the proliferation of the bacterium. The minimum inhibitory concentration (MIC) denotes the smallest concentration of a substance required to completely halt bacterial growth. All screened compounds demonstrated *in-vitro* inhibitory efficacy against Mtb, with MIC spanning from 1.56 to $\geq 25.0\text{ }\mu\text{g/mL}$ (Table 1). The series consists of 15 compounds, of which the BOK series has an additional amide functional group along with the carbonyl group with respect to the BOP series. The amide functional group was added to the tail portion of the molecule to study the effect on the potency of the molecule (Figure 1c). From the MIC evaluation, we could conclude that the addition of an amide functional group led to improved potency. The estimated MIC of BOP-1 was $5.9\text{ }\mu\text{g/mL}$, whereas the introduction of amide functionality increased the potency by approximately twofold (BOK-1 had an MIC of $3.2\text{ }\mu\text{g/mL}$). Similarly, the potency of BOK-5 was found to have increased by twofold compared to BOP-3 (MIC 11.6 vs $20.5\text{ }\mu\text{g/mL}$, respectively). The compounds BOK-2 and BOK-3 showed significant inhibitory potency against Mtb with MIC 1.8 and $2.4\text{ }\mu\text{g/mL}$, respectively. Both the compounds had an amide group and substitution at the ortho position of the phenyl ring (polar portion). In contrast, other

Table 1. Assessment of 1,2,3-triazole clubbed benzoxazole derivatives for *in-vitro* antitubercular evaluation (MIC₅₀), cytotoxicity (IC₅₀), selectivity index, and DprE1 inhibition assay.

S. no.	Compound	Mtb H37Rv MIC ₅₀ ($\mu\text{g/mL}$)	3T3 cell IC ₅₀ ($\mu\text{g/mL}$)	Selectivity index*	DprE1 inhibition assay IC ₅₀ (μM)
1.	BOK-1	3.2	118.5	37.07	5.2 ± 0.6
2.	BOK-2	1.8	103.92	57.77	2.2 ± 0.1
3.	BOK-3	2.4	112.1	46.75	3.0 ± 0.6
4.	BOK-4	6.9	ND	ND	ND
5.	BOK-5	11.6	ND	ND	ND
6.	BOK-6	39.6	ND	ND	ND
7.	BOK-7	6.7	ND	ND	ND
8.	BOK-8	44.1	ND	ND	ND
9.	BOK-9	10.6	ND	ND	ND
10.	BOK-10	42.6	ND	ND	ND
11.	BOP-1	5.9	51.69	8.76	3.3 ± 1.0
12.	BOP-2	19.06	ND	ND	ND
13.	BOP-3	20.5	ND	ND	ND
14.	BOP-4	4.8	55.8	11.62	3.1 ± 0.7
15.	BOP-5	32.3	ND	ND	ND
16.	TCA-1	ND	ND	ND	3.0 ± 0.2
17.	Rifampicin	< 0.004	ND	ND	ND
18.	5-Fluorouracil	ND	53.72	ND	ND

*Selectivity index = IC₅₀ ($\mu\text{g/mL}$)/MIC ($\mu\text{g/mL}$).

ND = Not done. The bold numbers represents compounds and standard drugs with significant activity.

compounds having substitutions on the meta and a few para positions of the phenyl ring such as BOK-4, BOK-7, and BOP-4 inhibited Mtb at concentrations i.e. 6.9, 6.7, and $4.8\text{ }\mu\text{g/mL}$, respectively. Other compounds featuring substitutions of ethoxy, trifluoromethyl, bromo, and nitro groups, positioned para to the phenyl ring showed activity $>25\text{ }\mu\text{g/mL}$ (Table 1).

Assessment of derivatives on mouse fibroblast 3T3-cell replication

In the early stages of drug discovery, potential candidates are typically tested against mammalian cell lines, such as mouse fibroblast 3T3 cells, to gauge any potential cytotoxic effects. The safety assessment of compounds BOK-1, BOK-2, BOK-3, BOP-1, and BOP-4, each exhibiting MIC values of $\leq 6.25\text{ }\mu\text{g/mL}$, was conducted using the MTT assay against mouse fibroblast 3T3 cells. The increase in cellular mortality implies a reduction in the enzymatic conversion of MTT dye to formazan within the mitochondria. Exposure to escalating concentrations (ranging from 3.13 to $200\text{ }\mu\text{g/mL}$) of test compounds during a 48-h incubation led to a concentration-dependent decline in cell vitality relative to the control group (Figure 3a). Our results reveal that concentrations of up to $50\text{ }\mu\text{g/mL}$ were permissible for all the compounds tested. Based on these observations, we extended the concentration range to $100\text{ }\mu\text{g/mL}$, as there was minimal inhibition observed, with values not even crossing 20%. In contrast, the cytotoxicity concentration for the standard, 5-fluorouracil, at $50\text{ }\mu\text{g/mL}$ exceeds 42% inhibition. The corresponding percentage inhibition data are presented in Table 1. The selectivity index (SI) is determined by the ratio between *in-vitro* cytotoxicity ($\mu\text{g/mL}$) and antimycobacterial activity ($\mu\text{g/mL}$). The compounds BOK-2 and BOK-3, which demonstrated the most promising antitubercular activity, exhibited an SI > 45 , indicating a substantial safety margin (Table 1).

DprE1 protein inhibition through the in-vitro DprE1 inhibition assay

For the identification and validation of the biological target for this new series of 1,2,3-triazole-linked benzoxazoles, compounds

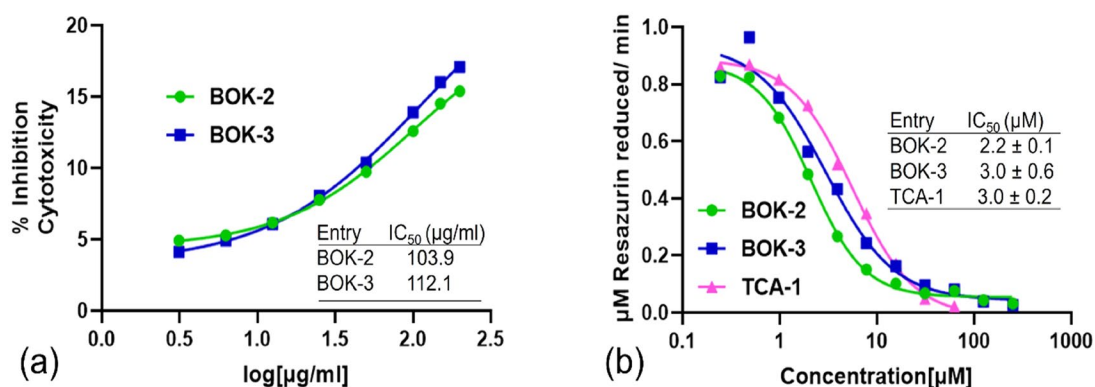


Figure 3. Assessment of synthesised compounds through *in-vitro* testing. (a) Effect of derivatives (3.13, 6.25, 12.5, 25, 50, 100, 150 and 200 µg/mL) on mouse fibroblast 3T3-cell proliferation showing IC₅₀ of 103.9 µg/mL (BOK-2) and 112.1 µg/mL (BOK-3). (b) DprE1 inhibitory concentration–response graph of derivatives BOK-2 and BOK-3 (0.24 to 250.00 µM) determined by the DprE1 inhibition assay.

Table 2. Molecular docking scores and DprE1 inhibition IC₅₀ values for synthesised compounds with different substitutions.

S.no.	Compound code	Substitution	Position of substitution	(-) CDOCKER energy	(-) CDOCKER interaction energy	DprE1 inhibition IC ₅₀ (µM)
1	BOK-1	H	–	36.04	52.16	5.2 ± 0.6
2	BOK-2	Methyl	Ortho	40.10	59.05	2.2 ± 0.1
3	BOK-3	Fluoro	Ortho	39.12	58.65	3.0 ± 0.6
4	BOP-1	H	–	28.18	48.12	3.3 ± 1.0
5	BOP-4	Fluoro	Para	28.11	47.36	3.1 ± 0.7
6	TCA-1	–	–	35.35	55.98	3.0 ± 0.2

displaying antimycobacterial activity below 6 µg/mL and showcasing diverse side chains were assessed against the purified DprE1 protein (Table 1). The assessment of the compounds' ability to inhibit DprE1 activity was conducted through an *in-vitro* assay. This involved purified DprE1 protein, geranylgeranyl-phosphoryl-β-d-ribose (GGPR) substrate, and resazurin as a redox indicator. The synthesised molecules were tested for their impact on DprE1 activity within this experimental setup. The initial rates of activity, characterised by increasing concentrations of the compound, were measured and compared to the control compound TCA-1. The half maximal inhibitory concentration (IC₅₀) was then calculated for each synthesised compound, quantitatively assessing their inhibitory effect. Compounds BOK-2 and BOK-3 (Figure 3b) significantly inhibited DprE1 protein with IC₅₀ values of 2.2 ± 0.1 µM and 3.0 ± 0.6 µM, respectively (see Fig. S47 of Supporting Information for the concentration-response graph of other compounds), demonstrating a strong correlation with the MIC values observed for the tested compounds. The promising results prompted us to delve deeper into these compounds through initial assessments of their druggability profiles and validation via computational studies. This approach aims to enhance our understanding of the structural features involved in the inhibition mechanism of the DprE1 enzyme, utilising docking and molecular dynamics (MD) simulation studies.

Exploration of binding affinity and intermolecular interactions via molecular docking analysis

Active compounds demonstrating IC₅₀ values within the range of TCA-1 were selected for docking studies within the DprE1 binding pocket. The primary objective of molecular docking analysis is to unravel the binding pose of molecules, providing insights into their inhibitory potency through an understanding of intermolecular interactions with the target protein. In docking studies, the

CDOCKER docking application, which utilises the CharmM force field, evaluates results based on -CDOCKER energy and -CDOCKER interaction energy²². -CDOCKER energy accounts for ligand internal strain and receptor–ligand interactions, while -CDOCKER interaction energy describes non-bonded interactions like van der Waals and electrostatic forces. Negative values for both energies indicate favourable binding between the protein and ligand^{23,24}. Remarkably, the synthesised compounds BOK-2 and BOK-3, which showed the maximum potency (IC₅₀), were also observed to bind to the active site, consistent with information documented in the RCSB crystallography database. These compounds exhibited maximum docking energy and interaction energy values of (–)59.05 and (–)58.65 kcal/mol, respectively (Table 2) (see Table S1 in the supplemental material for other compounds' molecular docking scores). To validate the docking protocol, we re-docked the most potent compound, revealing a minimal root mean square deviation (RMSD) value of 0.532 Å for the bioactive conformations²⁵. Through these studies, key amino acid residues, including Lys418, His132, Ser228, Cys387, and Gln334, have been identified as crucial for binding. Additional insights into how these residues contribute to forming hydrogen bonds and participating in hydrophobic interactions, can be found in the Supporting Information (see Fig. S46). In Figure 4, the alignment of essential amino acids with the designed ligands within the complex of DprE1 inhibition is depicted (see Fig. S48 of Supporting Information for further details). To enhance our comprehension of the dynamics and stability MD simulations were conducted.

Dynamic stability of DprE1 protein in complex with BOK-2 and BOK-3 along with cofactor FAD through MD simulation analysis

While docking offers a static view, MD offers a dynamic understanding by conducting long-range time-dependent studies confirming the binding pose observed in docking. The binding pose of the ligand is consistent with the reference molecule and is maintained throughout the MD simulation run. The study began with 300 ns production runs to observe the behaviour of ligand-free DprE1 protein and its complexes with BOK-2, BOK-3, and TCA-1, independently. Dynamics of active ligands within the DprE1 ligand binding domain (LBD), alongside cofactor FAD, were studied over time in a solvated environment²⁶. Superimposed structures at regular intervals (60th, 120th, 180th, 240th, and 300th ns) reveal conformational fluctuations in the presence of ligand (BOK-3) at the LBD, complemented by FAD binding (Figure 5). During simulations, the cofactor FAD remained intact, consistent with literature

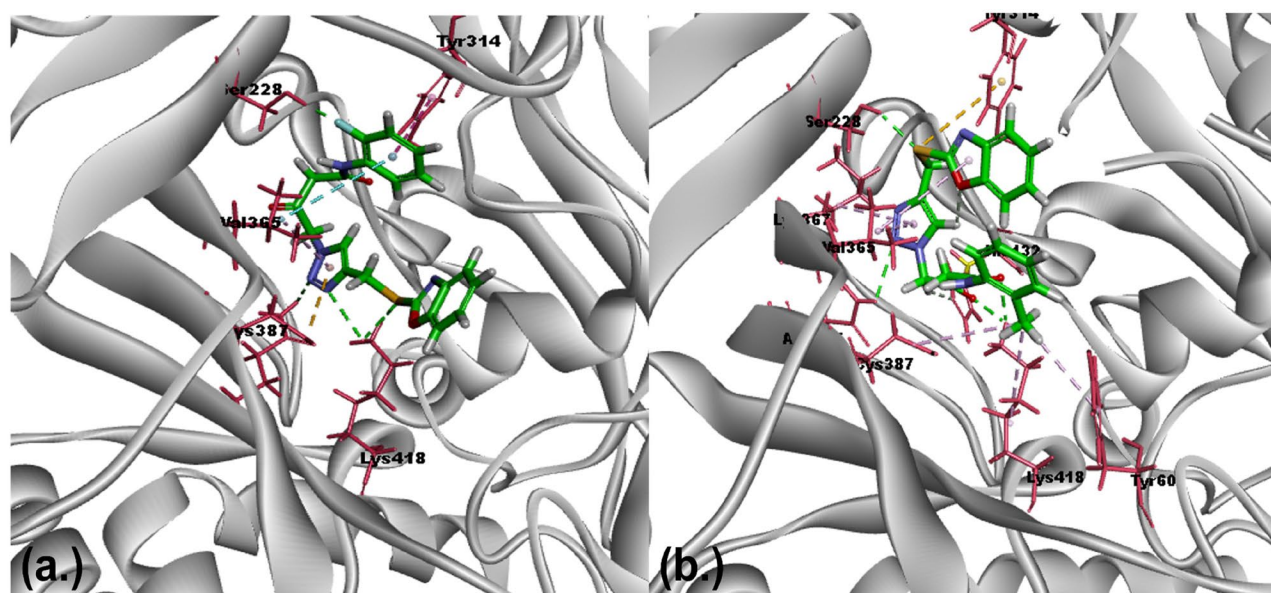


Figure 4. Assumed binding mode of DprE1 with ligands: molecular interactions with BOK-2 and BOK-3 (a) Molecular alignment of compound BOK-2 within the DprE1 binding pocket: exposing hydrogen bonding and hydrophobic interactions with amino acids His132, Ser228, Tyr314, Lys367, Val365, Asn385, Cys387, Tyr60, and Lys418. (b) Molecular alignment of compound BOK-3 within the DprE1 binding pocket: exposing hydrogen bonding and hydrophobic interactions with amino acids Tyr314, Ser228, Val365, Cys387, and Lys418.

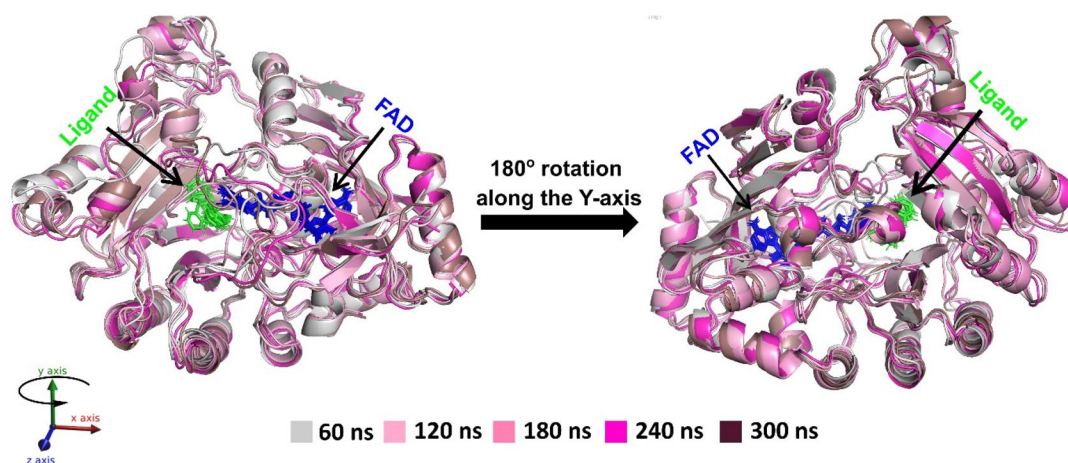


Figure 5. Superimposition of ligand (BOK-3) bound DprE1 protein along with FAD complex throughout trajectory in time-lapse at 60th, 120th, 180th, 260th, and 300th ns time step.

suggesting its complementary role in ligand binding to the LBD through intermolecular hydrogen bonds.

Trajectory analysis (Figure 6a and b) illustrates conformational changes, with structures superimposed in the absence and presence of ligand at intervals (60th, 180th, and 300th ns) (see Fig.S49 in the supplemental material for other time intervals). Initially, protein structures without and with ligands overlapped precisely, but larger deviations in RMSD values were observed as the MD run progressed, while the ligands, FAD binding pose, and secondary structures remained intact.

Analysis of RMSD (Figure 7c) reveals that the equilibrium of the C- α atoms for both unliganded and ligand-bound protein assemblies was reached around 75–90 ns, followed by stable trajectories with minimal deviation (0.10–0.15 nm), suggesting enhanced structural stability in ligand-bound protein assemblies. As per Figure 7d, the ligand-free protein showed reduced gyration

fluctuations (~ 0.15 nm) compared to the stable trajectories observed in the ligand-bound protein (~ 0.05 nm). Furthermore, the formation of intermolecular hydrogen bonds between ligands (BOK-2, BOK-3, and TCA-1) and LBD at different time frames indicated protein-ligand stability and biological responses^{25,27}. The hydrogen bond count remained constant over time, consistent with molecular docking results (Figure 7e). The solvent-accessible surface area (SASA) values (Figure 7f) consistently fluctuated within the range of 10–20 nm² approximately²⁸. Root Mean Square Fluctuation (RMSF) analysis (Figure 7g and h) revealed residue-wise fluctuations, with crucial amino acids exhibiting increased stiffness in the complex compared to the protein's native state. These findings are consistent with residues identified during the molecular docking experiment^{29–31}. Overall, the simulation outcomes provide valuable insights into how ligands (BOK-2 and BOK-3) interact with the DprE1 protein, revealing their bioactive characteristics.

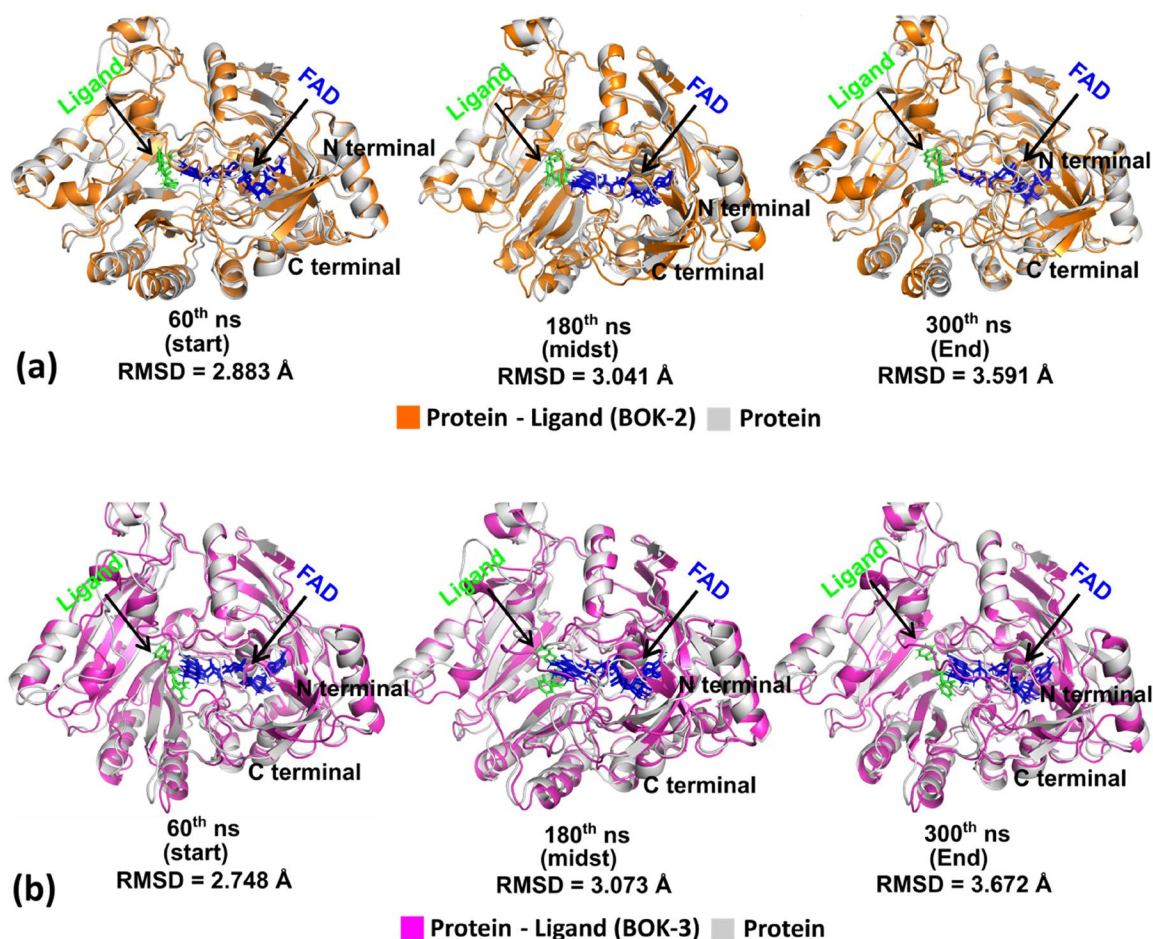


Figure 6. (a) and (b) Progressive superimposition of trajectory conformations of DprE1 complex with ligand-free protein and with ligands (**BOK-2** and **BOK-3**) at time points 60th, 180th, and 300th ns.

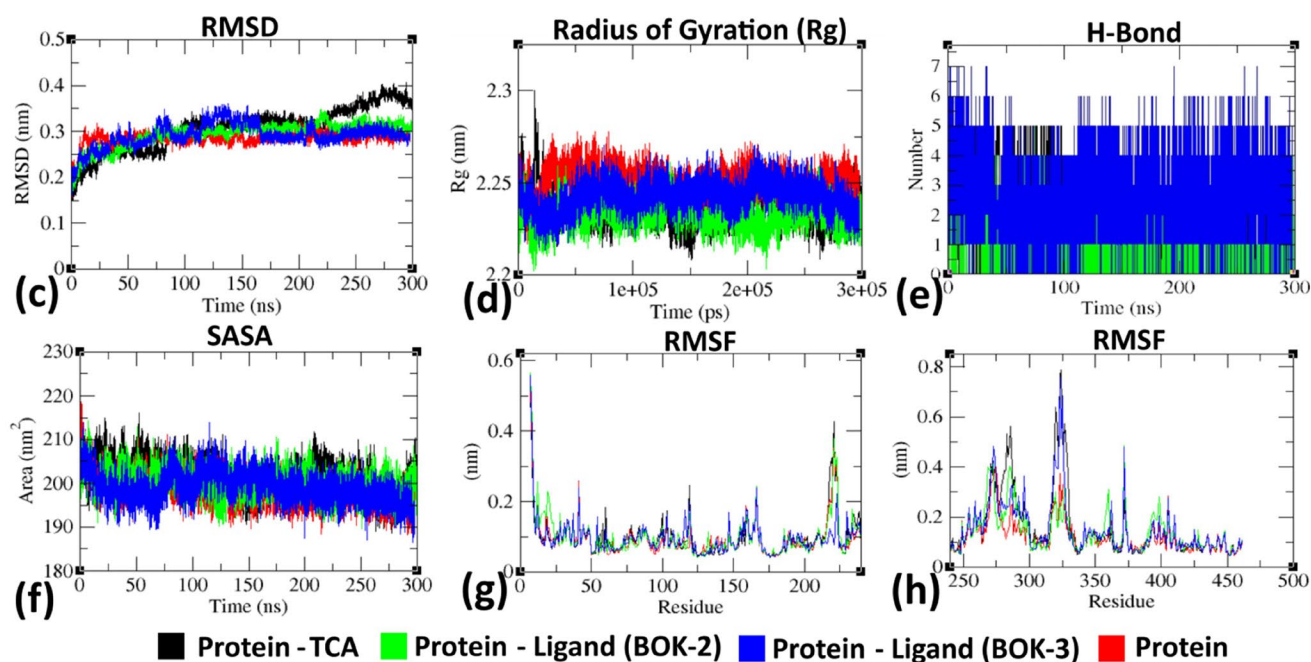


Figure 7. Evaluation of RMSD, Rg, hydrogen bond formation, SASA, and RMSF of DprE1 (protein) with BOK-2, BOK-3, and TCA-1 (ligand) complexes at 300,000 ps (300ns). (c) Temporal changes in backbone RMSD of DprE1 protein with and without ligand complexes. (d) Variation of protein backbone Rg between its unbound and complexed states throughout the simulation duration. The y-axis represents Rg (nm), while the x-axis depicts the time interval (ps). (e) Temporal evolution of hydrogen bonds between protein and ligand throughout simulation (ns) (f) Time-dependent SASA analysis. The y-axis represents SASA (nm²), while the x-axis denotes time (ns). (g) and (h) Comparison of residue-wise average RMSF plot between protein in native and ligand-bound states.

Computational drug-Likeness and ADMET prediction for safety evaluation

Ensuring optimal oral absorption and a favourable ADMET profile is crucial for drug success, reducing late-stage trial setbacks. Utilising computational tools like <http://www.swissadme.ch/>, we forecasted ADME attributes (Supporting Information, see Table S2) within the recommended ranges for 95% of known drugs. SMILES notation facilitated rapid predictions, encompassing gastrointestinal absorption, bioavailability, CYP enzyme inhibition, blood–brain barrier permeability, skin permeability, and pan-assay interference compounds (PAINS) alerts. Topological polar surface area (TPSA) indicates polarity impacting absorption and blood–brain barrier traversal, while iLOGP reflects solvation-free energy. ESOL LogS indicates hydrophilicity, and cytochrome-P450 isozymes influence metabolism and drug removal, with enzyme suppression leading to interactions, accumulation, and adverse effects. PAINS alerts aid in detecting false positives in drug discovery^{31,32}.

Among the synthesised compounds, no molecules exhibit violations in Lipinski's rule, indicating that these compounds were most probably orally active. The synthesised compounds were predicted to have logP values ranging from 2.07 to 3.29. As we are concerned with anti-tubercular potential, the logP value is a crucial parameter contributing to drug activity. The active drugs BOK-2 and BOK-3 reveal predicted logP values of 2.7 and 2.54, respectively, which is found to be better than the reference standard TCA-1 (1.81). Notably, the predicted blood–brain barrier penetration characteristics and PAINS alert were favourable for the synthesised compounds (supplementary data). Overall, these preliminary screening data suggested that the synthesised compounds can be promising drug candidates that can be taken forward for further evaluation in the drug discovery pipeline.

SAR analysis of 1,2,3-triazole clubbed benzoxazole derivatives

Piton et al.³² and Chikhale et al.⁶, extensively characterised DprE1 protein, revealing three distinct regions – head, trunk, and tail – based on ligand conformations (TCA-1). The binding pocket consistently houses FAD, supporting ligand binding. The head region forms a hydrophobic cavity, the trunk is flanked by FAD and specific residues, and the tail is flexible, featuring crucial amino acids. These insights deepen our understanding of DprE1's structure and guide potential drug-targeting strategies.

Inspired by DprE1's characterisation, we designed novel compounds with 1,2,3-triazole clubbed benzoxazole moieties (Figure 1c). Our efficient and cost-effective synthetic scheme ensures timely synthesis, combining structural innovation with practical considerations. *In-vitro* screening against Mtb H37Rv was conducted for compounds (3a–3j and 3k–3o), wherein their antimycobacterial activity was determined and reported as MIC₅₀ (minimum inhibitory concentration inhibiting 50% bacterial growth). For effective structure–activity relationship (SAR), variations in chain length and substitutions involving the phenyl moiety were introduced at the N-3 position of the triazole nucleus.

Introducing the amide group via ω -bromo acetoacetanilide (BOK series) enhanced antimycobacterial and DprE1 inhibition activity twofold compared to substituted phenacyl bromide (BOP series) (BOP-1: 5.9 μ g/mL, BOK-1: MIC 3.2 μ g/mL). Substitution patterns (ortho, meta, para) of the phenyl ring in the side chain influenced both activities. Ortho-substitution, as seen in BOK-2 (methyl at ortho), displayed superior activity (MIC 1.8 μ g/mL, IC₅₀ 2.0 μ M in DprE1 inhibition), while para-substitution, as in BOK-5 (methyl at para), showed lower activity (11.6 μ g/mL) and no enzyme

inhibition. BOK-3 (fluoro atom at ortho) demonstrated MIC 2.4 μ g/mL and IC₅₀ 3.0 μ M in DprE1 inhibition activity.

Furthermore, a comparison between BOK-4 (chloro at meta position) and BOK-7 (chloro at para position) highlights the favourable activity of meta-substitution over para-substitution. BOK-4 exhibited higher activity at 3.7 μ g/mL, while BOK-7 showed lower activity at 6.9 μ g/mL. Docking studies were conducted to elucidate the inhibition of the DprE1 enzyme by the synthesised compounds. The *in-silico* analysis reinforced the evidence that ortho-substitution is the most active. BOK-2 and BOK-3 displayed the highest -CDocker energy (40.1096 and 39.1274, respectively) and -CDocker interaction energy (59.0549 and 58.6535, respectively). These two ligands underwent simulation studies to assess stability under various physiological conditions.

Conclusions

In the present paper, we explore the potential of synthetic molecules to modulate DprE1, offering a promising new pathway for developing effective therapeutic interventions against tuberculosis. Until now, a limited number of scholarly publications have focused on leveraging the 1,2,3-triazole moiety to inhibit the DprE1 protein. We showcased an innovative synthetic scheme for the purposeful design of 15 1,2,3-triazole fused benzoxazole compounds (BOK-1–BOK-10 and BOP-1–BOP-5), employing the Cu(I)-catalysed cycloaddition method as a highly effective catalyst under mild conditions. The MIC against the Mtb H₃₇R_v strain was determined using the REMA assay for the newly synthesised derivatives. The SAR analysis highlighted that introducing the amide moiety in the BOK series resulted in improved antimycobacterial activity. Amongst all the compounds, BOK-2 and BOK-3 showed significant anti-TB activity with MIC i.e. 1.8 and 2.4 μ g/mL, respectively. Upon evaluating the DprE1 inhibitory activity, compounds BOK-2 and BOK-3 demonstrated IC₅₀ values of 2.2 \pm 0.1 and 3.0 \pm 0.6 μ M, respectively, as compared to the standard drug TCA-1 (IC₅₀ = 3.0 \pm 0.2 μ M). The *in-silico* results were also aligned with the outcomes of the biochemical assessments. The docking studies not only suggested the binding pose of protein–ligand interaction but also highlighted the crucial amino acids involved in pivotal binding interactions, including Lys418, His132, Ser228, Cys387, and Gln334, like the literature-reported molecule (TCA-1). The MD simulation study conducted for 300 ns validated the docking study and provided valuable structural insights highlighting the stability of the protein–ligand complex.

Experimental section

Chemistry

All the chemicals and solvents were procured from Sigma-Aldrich and used without further purification. Intermediates and final products were verified for purity using thin-layer chromatography (TLC), IR, ¹H NMR, ¹³C NMR, and mass spectroscopy. TLC analysis employed Kieselgel 60 F254 aluminium sheets with solvent system of n-hexane/ethyl acetate/methanol (3:2:0.5). Melting points were determined using standard apparatus and were reported without correction. IR spectra were obtained using KBr pellets with a Shimadzu FTIR 8400-S spectrophotometer. LC/MS spectra were acquired with electrospray (ES) ionisation at –70 eV. NMR spectra were recorded in dimethylsulphoxide (DMSO)-d₆ at 298 K using a Bruker 400 MHz FT-NMR spectrophotometer with reference to DMSO-d₆ at δ H 2.50 ppm for proton NMR and δ C 39.5 ppm for

carbon NMR. Resonance patterns were characterised as s (singlet), d (doublet), t (triplet), q (quartet), or m (multiplet), with additional coupling constants (J) provided.

Substituted acetoacetanilide synthesis (1a–1j)

A solution containing ethyl acetoacetate (0.01 M) and substituted aniline (0.01 M) was prepared and subjected to reflux for approximately 2–3 h. Following the reflux, the resulting yellowish/brown liquid was further heated on a water bath to eliminate the alcohol by-product generated during the reaction³³. After allowing the reaction solution to reach ambient temperature, the crude solid product was obtained by filtration and washed with ether. The purification process involved recrystallization, utilising a solution comprising 25% alcohol in water^{33,34}. The yields proved quite promising, with results ranging from 68% to 98% as white to colourless crystals.

ω -bromoacetoacetanilides synthesis (2a–2j)

In a reaction vessel, a mixture comprising 0.022 M of substituted acetoacetanilide dissolved in 12 ml of glacial acetic acid underwent gradual addition of a bromine solution. This solution, consisting of 0.022 M of bromine, dissolved in 17 ml of glacial acetic acid and containing a small crystal of iodine^{17,21} was added slowly over the course of 1 h at ambient temperature. After the addition, the solution was further stirred for an additional 6–8 h until the reaction reaches completion, confirmed by TLC analysis. Subsequently, the solution was poured into water, resulting in the formation of ω -bromo substituted acetoacetanilides³⁵. The product was isolated by crystallisation, using ethanol as the solvent, yielding a white amorphous product with a yield of 85%–90%.

Synthesis of thiopropargylated benzoxazole (iv)

A solution consisting of 10 mM of 2-mercapto benzoxazole dissolved in 30 ml of absolute ethanol, along with 12 mM of triethylamine (Et₃N) and 12 mM of propargyl bromide, was introduced with continuous stirring. The resulting mixture was then heated to 90 °C for a duration of 1 h. The surplus solvent was then evaporated using a rotary evaporator. Afterwards, the solid product obtained underwent a thorough washing procedure with cold water. Finally, it was subjected to recrystallization from ethanol, resulting in the isolation of the compound in a high yield of 94%, forming colourless crystals.

Synthesis of 1,2,3-triazole clubbed benzoxazole acetoacetanilide/phenacyl derivatives (3a–3j and 3k–3o)

In a round bottom flask, a solution containing thiopropargylated benzoxazole (1 M equiv), substituted ω -bromo acetoacetanilide/substituted phenacyl bromide (1 M equiv), and sodium azide (1.1 M equiv) in a mixture of DMF and H₂O in a 1:1 (v/v) ratio was prepared. To this blend, CuSO₄·5H₂O (0.15 M equiv) and sodium ascorbate (0.30 M equiv) were introduced³⁶. The ensuing solution was agitated at ambient temperature for 8–12 h, while the reaction advancement was tracked using TLC. After the completion of the reaction, the solution was cooled, and the reaction was halted by pouring it into ice water³⁷. The resultant solid product was isolated via filtration and rinsed with water. Following this, the product underwent recrystallization from ethanol, yielding 82%–95%.

4–(4–((Benzo[d]oxazol-2-ylthio)methyl)-1H-1,2,3-triazol-1-yl)-3-oxo-N-phenyl butanamide(3a) (see Fig. S1,S2,S3): Light brown solid,

yield 85%, m.p.: 161 °C–165 °C, FTIR ν_{\max} (KBr, cm⁻¹): 3366.20 (N–H str.), 3153.26 (C–H str., triazole ring), 2891.42 (C–H str., al), 1707.06 (C=O), 1663.20 (C=O str., amide), 1510.30, 1452.34 (C=C str., Ar), 697.50 (C–S str.) cm⁻¹. ¹H NMR (δ ppm, DMSO-d₆): 3.726 (s, 2H, CH₂), 4.719 (s, 2H, CH₂), 5.600 (s, 2H, CH₂), 7.070 (t, 1H, ArH, J=7.6 Hz), 7.080 (t, 2H, ArH, J=7.6 Hz), 7.317 (t, 1H, ArH, J=7.6 Hz), 7.335 (t, 1H, ArH, J=7.6 Hz), 7.550 (d, 2H, ArH, J=7.6 Hz), 7.569 (d, 1H, ArH, J=2.8 Hz), 7.668 (d, 1H, ArH, J=6.8 Hz), 8.086 (s, 1H, CH), 10.167 (s, 1H, NH). ¹³C NMR (δ ppm, DMSO-d₆): 26.890, 49.282, 58.641, 110.742, 118.847, 119.404, 119.644, 124.087, 124.870, 125.135, 128.910, 129.265, 139.111, 141.676, 151.813, 164.813, 164.801, 197.905. MS (m/z): M+1 analysed 408.12, M+1 predicted 408.46.

4–(4–((Benzo[d]oxazol-2-ylthio)methyl)-1H-1,2,3-triazol-1-yl)-3-oxo-N-(o-tolyl) butanamide(3b) (see Fig. S4,S5,S6): Light brown solid, yield: 89%; m.p.: 172 °C–176 °C; FTIR ν_{\max} (KBr, cm⁻¹): 3357.60 (N–H str.), 3134.20 (C–H str., triazole ring), 2871.32 (C–H str., al), 1710.16 (C=O), 1643.70 (C=O str., amide), 1520.20, 1472.14 (C=C str., Ar), 687.43 (C–S str.) cm⁻¹. ¹H NMR (δ ppm, DMSO-d₆): 2.192 (s, 3H, CH₃), 3.756 (s, 2H, CH₂), 4.720 (s, 2H, CH₂), 5.597 (s, 2H, CH₂), 7.093 (d, 1H, ArH, J=6.4 Hz), 7.183 (d, 1H, ArH, J=7.2 Hz), 7.223 (t, 1H, ArH, J=7.2 Hz), 7.347 (t, 1H, ArH, J=6.0 Hz), 7.406 (t, 1H, ArH, J=7.6 Hz), 7.425 (t, 1H, ArH, J=7.6 Hz), 7.656 (d, 1H, ArH, J=6.4 Hz), 7.672 (d, 1H, ArH, J=6.4 Hz), 8.098 (s, 1H, CH), 9.524 (s, 1H, NH). ¹³C NMR (δ ppm, DMSO-d₆): 18.240, 26.909, 48.642, 58.620, 110.749, 118.857, 124.890, 124.995, 125.146, 125.337, 125.898, 126.436, 130.756, 130.812, 132.039, 136.262, 141.665, 151.808, 164.642, 165.800, 198.136. MS (m/z): M+1 analysed 422.13, M+1 predicted 422.48.

4–(4–((Benzo[d]oxazol-2-ylthio)methyl)-1H-1,2,3-triazol-1-yl)-N-(2-fluorophenyl)-3-oxobutanamide(3c) (see Fig. S7,S8,S9): Light brown solid, yield: 91%; m.p.: 175 °C–179 °C; FTIR ν_{\max} (KBr, cm⁻¹): 3417.10 (N–H str.), 3124.40 (C–H str., triazole ring), 2861.62 (C–H str., al), 1712.10 (C=O), 1653.60 (C=O str., amide), 1530.10, 1462.24 (C=C str., Ar), 689.13 (C–S str.) cm⁻¹. ¹H NMR (δ ppm, DMSO-d₆): 3.810 (s, 2H, CH₂), 4.726 (s, 2H, CH₂), 5.582 (s, 2H, CH₂), 7.010 (t, 1H, ArH, J=7.2 Hz), 7.161 (t, 1H, ArH, J=6.0 Hz), 7.263 (d, 1H, ArH, J=7.2 Hz), 7.339 (t, 1H, ArH, J=7.6 Hz), 7.364 (t, 1H, ArH, J=7.6 Hz), 7.656 (d, 1H, ArH, J=4.4 Hz), 7.667 (d, 1H, ArH, J=4.4 Hz), 7.963 (d, 1H, ArH, J=6.4 Hz), 8.095 (s, 1H, CH), 9.980 (s, 1H, NH). ¹³C NMR (δ ppm, DMSO-d₆): 26.888, 48.884, 58.506, 110.754, 115.825, 116.016, 118.851, 123.994, 124.858, 125.137, 125.751, 125.827, 126.235, 126.347, 141.715, 151.835, 154.863, 164.130, 165.152, 197.927. MS (m/z): M+1 analysed 426.10, M+1 predicted 426.44.

4–(4–((Benzo[d]oxazol-2-ylthio)methyl)-1H-1,2,3-triazol-1-yl)-N-(3-chlorophenyl)-3-oxobutanamide(3d) (see Fig. S10,S11,S12): Light brown solid, yield: 92%; m.p.: 165 °C–169 °C; FTIR ν_{\max} (KBr, cm⁻¹): 3347.80 (N–H str.), 3124.80 (C–H str., triazole ring), 2881.22 (C–H str., al), 1718.10 (C=O), 1665.10 (C=O str., amide), 1542.10, 1481.18 (C=C str., Ar), 692.33 (C–S str.) cm⁻¹. ¹H NMR (δ ppm, DMSO-d₆): 3.740 (s, 2H, CH₂), 4.726 (s, 2H, CH₂), 5.604 (s, 2H, CH₂), 7.148 (d, 1H, ArH, J=7.6 Hz), 7.350 (d, 1H, ArH, J=8.0 Hz), 7.370 (t, 1H, ArH, J=8.0 Hz), 7.382 (t, 2H, ArH, J=4.8 Hz), 7.402 (t, 1H, ArH, J=8.0 Hz), 7.656 (d, 1H, ArH, J=8.2 Hz), 7.677 (d, 1H, ArH, J=8.4 Hz), 7.799 (s, 1H, CH), 8.082 (s, 2H, CH₂), 10.357 (s, 1H, NH). ¹³C NMR (δ ppm, DMSO-d₆): 26.885, 49.292, 58.608, 110.750, 118.007, 118.851, 119.119, 123.800, 124.864, 125.135, 131.007, 133.584, 140.531, 141.691, 151.823, 164.184, 165.064, 197.711. MS (m/z): M+1 analysed 442.07, M+1 predicted 442.44.

4-(4-((Benzo[d]oxazol-2-ylthio)methyl)-1H-1,2,3-triazol-1-yl)-3-oxo-N-(p-tolyl) butanamide(3e) (see Fig. S13,S14,S15): Light brown solid, yield: 91%; m.p.: 175°C–179°C; FTIR ν_{\max} (KBr, cm^{-1}): 3317.70(N–H str.), 3164.40 (C–H str., triazole ring), 2901.22 (C–H str.,al), 1716.19 (C=O), 1654.50 (C=O str.,amide), 1531.20, 1467.04 (C=C str., Ar), 690.03 (C–S str.) cm^{-1} . ^1H NMR (δ ppm, DMSO- d_6): 2.245 (s, 3H, CH_3), 3.715 (s, 2H, CH_2), 4.723 (s, 2H, CH_2), 5.606 (s, 2H, CH_2), 7.105 (d, 2H, ArH, $J=8.4\text{Hz}$), 7.324 (t, 1H, ArH, $J=7.2\text{Hz}$), 7.338 (t, 1H, ArH, $J=7.2\text{Hz}$), 7.441 (d, 2H, ArH, $J=8.4\text{Hz}$), 7.460 (d, 1H, ArH, $J=6.4\text{Hz}$), 7.662(d, 1H, ArH, $J=6.4\text{Hz}$), 8.085(s, 1H, CH), 10.091(s, 1H, NH). ^{13}C NMR (δ ppm, DMSO- d_6): 20.889, 26.849, 49.238, 58.656, 110.726, 118.837, 119.673, 120.272, 124.863, 125.124, 125.871, 129.622, 133.058, 136.612, 141.663, 151.798, 164.213, 164.375, 197.961. MS (m/z): M+1 analysed 422.13, M+1 predicted 415.13.

4-(4-((Benzo[d]oxazol-2-ylthio)methyl)-1H-1,2,3-triazol-1-yl)-3-oxo-N-(4-(trifluoromethyl) phenyl)butanamide (3f) (see Fig. S16,S17,S18): Light brown solid, yield: 84%; m.p.: 185°C–189°C; FTIR ν_{\max} (KBr, cm^{-1}): 3417.50(N–H str.), 3214.10 (C–H str., triazole ring), 2907.39 (C–H str.,al), 1740.17 (C=O), 1683.20 (C=O str.,amide), 1537.30, 1492.10 (C=C str., Ar), 691.13 (C–S str.) cm^{-1} . ^1H NMR (δ ppm, DMSO- d_6): 3.778 (s, 2H, CH_2), 4.718 (s, 1H, CH_2), 5.603 (s, 2H, CH_2), 7.346 (d, 2H, ArH, $J=7.6\text{Hz}$), 7.375 (d, 2H, ArH, $J=7.6\text{Hz}$), 7.664 (t, 1H, ArH, $J=7.2\text{Hz}$), 7.705 (t, 1H, ArH, $J=7.2\text{Hz}$), 7.768 (d, 1H, ArH, $J=8.2\text{Hz}$), 7.790 (d, 1H, ArH, $J=8.4\text{Hz}$), 8.064 (s, 1H, CH), 10.536 (s, 1H, NH). ^{13}C NMR (δ ppm, DMSO- d_6): 26.885, 49.354, 58.582, 110.746, 118.845, 119.534, 124.835, 124.602, 125.123, 125.717, 126.596, 126.633, 141.730, 142.688, 142.773, 151.843, 164.101, 165.349, 197.721. MS (m/z): M+1 analysed 476.10, M+1 predicted 476.09.

4-(4-((Benzo[d]oxazol-2-ylthio)methyl)-1H-1,2,3-triazol-1-yl)-N-(4-chlorophenyl)-3-oxo butanamide(3g) (see Fig. S19,S20,S21): Light brown solid, yield: 89%; m.p.: 171°C–174°C; FTIR ν_{\max} (KBr, cm^{-1}): 3350.41(N–H str.), 3129.30 (C–H str., triazole ring), 2931.42 (C–H str.,al), 1721.11 (C=O), 1639.84 (C=O str.,amide), 1541.10, 1487.10 (C=C str., Ar), 689.49 (C–S str.) cm^{-1} . ^1H NMR (δ ppm, DMSO- d_6): 3.728 (s, 2H, CH_2), 4.720 (s, 2H, CH_2), 5.597 (s, 2H, CH_2), 7.361 (t, 1H, ArH, $J=6.8\text{Hz}$), 7.378 (t, 1H, ArH, $J=6.8\text{Hz}$), 7.381 (d, 2H, ArH, $J=8.0\text{Hz}$), 7.577 (d, 1H, ArH, $J=8.0\text{Hz}$), 7.597 (d, 2H, ArH, $J=8.0\text{Hz}$), 7.665 (d, 1H, ArH, $J=8.0\text{Hz}$), 8.086 (s, 1H, CH), 10.303 (s, 1H, NH). ^{13}C NMR (δ ppm, DMSO- d_6): 26.846, 49.237, 58.644, 110.746, 118.838, 121.206, 124.892, 125.141, 126.078, 127.647, 129.181, 138.049, 140.052, 141.643, 151.788, 164.269, 164.798, 197.767. MS (m/z): M+1 analysed 442.09, M+1 predicted 442.06.

4-(4-((Benzo[d]oxazol-2-ylthio)methyl)-1H-1,2,3-triazol-1-yl)-N-(4-bromophenyl)-3-oxo butanamide(3h) (see Fig. S22,S23,S24): Light brown solid, yield: 82%; m.p.: 210°C–214°C; FTIR ν_{\max} (KBr, cm^{-1}): 3367.67(N–H str.), 3224.10 (C–H str., triazole ring), 2969.02 (C–H str.,al), 1780.06 (C=O), 1671.42 (C=O str.,amide), 1567.51, 1482.24 (C=C str., Ar), 688.40 (C–S str.) cm^{-1} . ^1H NMR (δ ppm, DMSO- d_6): 3.725 (s, 2H, CH_2), 4.717 (s, 2H, CH_2), 5.591 (s, 2H, CH_2), 7.349 (d, 2H, ArH, $J=7.4\text{Hz}$), 7.357 (t, 1H, ArH, $J=6.6\text{Hz}$), 7.374 (t, 1H, ArH, $J=6.6\text{Hz}$), 7.521 (d, 2H, ArH, $J=7.4\text{Hz}$), 7.662 (d, 1H, ArH, $J=4.8\text{Hz}$), 7.674 (d, 1H, ArH, $J=5.0\text{Hz}$), 8.064 (s, 1H, CH), 10.292 (s, 1H, NH). ^{13}C NMR (δ ppm, DMSO- d_6): 26.896, 49.281, 58.633, 110.733, 115.669, 118.827, 121.573, 122.912, 123.852, 124.858, 125.122, 132.087, 138.481, 141.671, 151.810, 164.206, 164.824, 197.762. MS (m/z): M+1 analysed 486.04, M+1 predicted 486.34.

4-(4-((Benzo[d]oxazol-2-ylthio)methyl)-1H-1,2,3-triazol-1-yl)-N-(4-methoxyphenyl)-3-oxo butanamide(3i) (see Fig. S25,S26,S27): Light brown solid, yield: 87%; m.p.: 169°C–172°C; FTIR ν_{\max} (KBr, cm^{-1}): 3347.55(N–H str.), 3124.22 (C–H str., triazole ring), 2869.12 (C–H str.,al), 1712.30 (C=O), 1653.41 (C=O str.,amide), 1537.39, 1491.14 (C=C str., Ar), 682.73 (C–S str.) cm^{-1} . ^1H NMR (δ ppm, DMSO- d_6): 3.685 (s, 3H, CH_3), 3.720 (s, 2H, CH_2), 4.717 (s, 2H, CH_2), 5.594 (s, 2H, CH_2), 6.901(d, 2H, ArH, $J=8.4\text{Hz}$), 7.344 (t, 1H, ArH, $J=7.2\text{Hz}$), 7.458 (d, 2H, ArH, $J=8.4\text{Hz}$), 7.480 (t, 1H, ArH, $J=7.2\text{Hz}$), 7.656 (d, 1H, ArH, $J=6.4\text{Hz}$), 7.671 (d, 1H, ArH, $J=6.4\text{Hz}$), 8.076 (s, 1H, CH), 10.303(s, 1H, NH). ^{13}C NMR (δ ppm, DMSO- d_6): 26.876, 49.135, 55.623, 58.637, 110.746, 112.493, 114.367, 118.846, 121.241, 124.871, 125.140, 130.644, 132.248, 141.676, 151.814, 155.910, 164.086, 164.185, 197.992. MS (m/z): M+1 analysed 438.13, M+1 predicted 438.47.

4-(4-((Benzo[d]oxazol-2-ylthio)methyl)-1H-1,2,3-triazol-1-yl)-N-(4-ethoxyphenyl)-3-oxo butanamide(3j) (see Fig. S28,S29,S30): Light brown solid, yield: 93%; m.p.: 175°C–179°C; FTIR ν_{\max} (KBr, cm^{-1}): 3357.60 (N–H str.), 3134.20 (C–H str., triazole ring), 2871.32 (C–H str.,al), 1710.16 (C=O), 1643.70 (C=O str., amide), 1520.20, 1472.14 (C=C str., Ar), 687.43 (C–S str.) cm^{-1} . ^1H NMR (δ ppm, DMSO- d_6): 1.305 (t, 3H, CH_3), 3.682 (s, 2H, CH_2), 3.987 (m, 2H, CH_2), 4.716 (s, 2H, CH_2), 5.591 (s, 2H, CH_2), 6.884 (d, 2H, ArH, $J=8.4\text{Hz}$), 7.336 (t, 1H, ArH, $J=4.0\text{Hz}$), 7.346 (t, 1H, ArH, $J=4.0\text{Hz}$), 7.424 (d, 2H, ArH, $J=8.4\text{Hz}$), 7.468 (d, 1H, ArH, $J=8.4\text{Hz}$), 7.676 (d, 1H, ArH, $J=8.0\text{Hz}$), 8.066 (s, 1H, CH), 10.018 (s, 1H, NH). ^{13}C NMR (δ ppm, DMSO- d_6): 15.120, 26.895, 49.165, 58.632, 63.555, 110.731, 114.886, 114.966, 118.824, 121.234, 124.849, 125.119, 125.832, 132.168, 141.685, 151.817, 155.181, 164.061, 164.177, 197.988. MS (m/z): M+1 analysed 452.15, M+1 predicted 452.50.

2-(4-((Benzo[d]oxazol-2-ylthio)methyl)-1H-1,2,3-triazol-1-yl)-1-phenylethan-1-one (3k) (see Fig. S31,S32,S33): White solid, yield: 90%; m.p.: 135°C–139°C; FTIR ν_{\max} (KBr, cm^{-1}): 3029.80 (C–H str., triazole ring), 2842.52 (C–H str.,al), 1653.12 (C=O str.), 1552.12, 1469.31 (C=C str., Ar), 689.19 (C–S str.) cm^{-1} . ^1H NMR (δ ppm, DMSO- d_6): 4.791 (s, 2H, CH_2), 6.202 (s, 2H, CH_2), 7.341 (t, 1H, ArH, $J=7.6\text{Hz}$), 7.593 (t, 2H, ArH, $J=7.6\text{Hz}$), 7.612 (t, 1H, ArH, $J=7.6\text{Hz}$), 7.659 (d, 1H, ArH, $J=2.8\text{Hz}$), 7.674 (d, 1H, ArH, $J=6.0\text{Hz}$), 7.726 (t, 1H, ArH, $J=7.6\text{Hz}$), 8.055 (d, 2H, ArH, $J=7.6\text{Hz}$), 8.212 (s, 1H, CH). ^{13}C NMR (δ ppm, DMSO- d_6): 26.795, 56.629, 110.772, 118.893, 125.017, 125.117, 126.370, 128.617, 129.435, 134.481, 134.727, 141.494, 143.385, 151.670, 164.626, 192.401. MS (m/z): M+1 analysed 351.19, M+1 predicted 351.39.

2-(4-((Benzo[d]oxazol-2-ylthio)methyl)-1H-1,2,3-triazol-1-yl)-1-(4-methoxyphenyl)ethan-1-one (3l) (see Fig. S34,S35,S36): White solid, yield: 86%; m.p.: 148°C–152°C; FTIR ν_{\max} (KBr, cm^{-1}): 3084.30 (C–H str., triazole ring), 2886.02 (C–H str.,al), 1674.15 (C=O str.), 1582.42, 1474.31 (C=C str., Ar), 683.99 (C–S str.) cm^{-1} . ^1H NMR (δ ppm, DMSO- d_6): 3.868 (s, 3H, CH_3), 4.749 (s, 2H, CH_2), 6.099 (s, 2H, CH_2), 7.117 (d, 2H, ArH, $J=8.8\text{Hz}$), 7.330 (d, 1H, ArH, $J=2.8\text{Hz}$), 7.345 (d, 1H, ArH, $J=2.0\text{Hz}$), 7.359 (t, 1H, ArH, $J=7.2\text{Hz}$), 7.661 (t, 1H, ArH, $J=7.2\text{Hz}$), 8.035 (d, 2H, ArH, $J=8.8\text{Hz}$), 8.146 (s, 1H, CH). ^{13}C NMR (δ ppm, DMSO- d_6): 26.963, 56.054, 56.144, 110.751, 114.668, 118.835, 124.859, 125.133, 126.132, 127.389, 131.023, 141.693, 142.795, 151.819, 164.209, 164.365, 190.739. MS (m/z): M+1 analysed 381.19, M+1 predicted 381.42.

2-(4-((Benzo[d]oxazol-2-ylthio)methyl)-1H-1,2,3-triazol-1-yl)-1-(p-tolyl)ethan-1-one(3m) (see Fig. S37,S38,S39): White solid, yield:

87%; m.p.: 142°C–146°C; FTIR ν_{\max} (KBr, cm^{-1}): 3073.14 (C–H str., triazole ring), 2840.27 (C–H str., al), 1683.12 (C=O str.), 1544.32, 1445.19 (C=C str., Ar), 687.19 (C–S str.) cm^{-1} . ^1H NMR (δ ppm, DMSO- d_6): 2.400 (s, 3H, CH_3), 4.747 (s, 2H, CH_2), 6.122 (s, 2H, CH_2), 7.355 (t, 1H, ArH, $J=7.6\text{Hz}$), 7.400 (d, 2H, ArH, $J=8.0\text{Hz}$), 7.657 (d, 1H, ArH, $J=7.8\text{Hz}$), 7.678 (d, 1H, ArH, $J=7.4\text{Hz}$), 7.696 (t, 1H, ArH, $J=7.6\text{Hz}$), 7.946 (d, 2H, ArH, $J=8.0\text{Hz}$), 8.154 (s, 1H, CH). ^{13}C NMR (δ ppm, DMSO- d_6): 21.723, 26.870, 56.309, 110.757, 118.864, 124.914, 125.160, 126.141, 128.704, 128.921, 129.971, 132.010, 141.639, 145.349, 151.781, 164.274, 191.954. MS (m/z): M+1 analysed 365.16, M+1 predicted 365.43.

2-(4-((Benzo[d]oxazol-2-ylthio)methyl)-1H-1,2,3-triazol-1-yl)-1-(4-fluorophenyl)ethan-1-one (3n) (see Fig. S40, S41, S42): White solid, yield: 86%; m.p.: 145°C–149°C; FTIR ν_{\max} (KBr, cm^{-1}): 3054.30 (C–H str., triazole ring), 2871.11 (C–H str., al), 1623.22 (C=O str.), 1526.12, 1459.84 (C=C str., Ar), 692.09 (C–S str.) cm^{-1} . ^1H NMR (δ ppm, DMSO- d_6): 4.759 (s, 2H, CH_2), 6.173 (s, 2H, CH_2), 7.347 (t, 1H, ArH, $J=8.8\text{Hz}$), 7.443 (t, 1H, ArH, $J=8.8\text{Hz}$), 7.665 (d, 1H, ArH, $J=8.0\text{Hz}$), 7.668 (d, 1H, ArH, $J=8.0\text{Hz}$), 8.137 (d, 2H, ArH, $J=8.8\text{Hz}$), 8.150 (d, 2H, ArH, $J=8.4\text{Hz}$), 8.166 (s, 1H, CH). ^{13}C NMR (δ ppm, DMSO- d_6): 26.923, 52.382, 110.729, 116.415, 116.634, 118.849, 124.855, 125.115, 126.102, 131.292, 131.320, 131.679, 131.775, 141.679, 151.806, 164.226, 164.763, 167.278, 191.182. MS (m/z): M+1 analysed 369.17, M+1 predicted 369.38.

2-(4-((Benzo[d]oxazol-2-ylthio)methyl)-1H-1,2,3-triazol-1-yl)-1-(4-nitrophenyl)ethan-1-one (3o) (see Fig. S43, S44, S45): Light pink solid, yield: 81%; m.p.: 142°C–146°C; FTIR ν_{\max} (KBr, cm^{-1}): 3341.20 (C–H str., triazole ring), 2891.16 (C–H str., al), 1632.62 (C=O str.), 1534.52, 1478.21 (C=C str., Ar), 681.4 (C–S str.) cm^{-1} . ^1H NMR (δ ppm, DMSO- d_6): 4.753 (s, 2H, CH_2), 6.246 (s, 2H, CH_2), 7.354 (t, 1H, ArH, $J=3.2\text{Hz}$), 7.384 (t, 1H, ArH, $J=3.2\text{Hz}$), 7.671 (d, 1H, ArH, $J=7.6\text{Hz}$), 7.691 (d, 1H, ArH, $J=7.2\text{Hz}$), 8.143 (s, 1H, CH), 8.286 (d, 2H, ArH, $J=9.2\text{Hz}$), 8.416 (d, 2H, ArH, $J=8.6\text{Hz}$). ^{13}C NMR (δ ppm, DMSO- d_6): 26.927, 56.810, 110.758, 118.851, 124.432, 124.864, 125.141, 125.949, 129.701, 130.112, 139.216, 141.713, 150.886, 151.837, 164.144, 191.988. MS (m/z): M+1 analysed 396.16, M+1 predicted 396.39.

Biological evaluation

Determination of MIC using REMA method

To begin, master solutions of each compound were prepared at a concentration of 10,000 $\mu\text{g}/\text{mL}$ using DMSO to ensure sterility. Subsequently, a dilution plate was set up from these master solutions, achieving a final compound concentration of 100 $\mu\text{g}/\text{mL}$. Next, a 96-well plate was set up for MIC determination. In every well, 100 μL of Middlebrook 7H9 broth enriched with 10% oleic acid, albumin, dextrose, and catalase was dispensed, except for the control wells. In the compound control, 150 μL was added, and in the medium control, 200 μL was added³⁷. Each compound was added in 100 μL volumes, undergoing serial dilutions. Concurrently, a suspension of MTB H37Rv (ATCC 27294) was prepared to achieve a density of 3×10^6 CFU/mL. From this mixture, 100 μL was dispensed into every well of the 96-well plate, excluding control wells, establishing an initial concentration of 25 $\mu\text{g}/\text{mL}$ for each compound. Following this, the plates were placed in a 5% CO_2 atmosphere and incubated at 37°C for 7 days. After incubation, 30 μL of 0.01% resazurin, dissolved in sterile distilled water, was added to every well. Following a 24-h incubation, fluorescence intensity was measured using the Biotek[®] Synergy H1 device. The

MIC90, representing the concentration causing a 90% reduction in bacterial growth, was derived from these measurements. This assay was conducted in triplicate, and the reported result represents the average of the three independent trials^{38,39}.

Cytotoxicity assay

Mouse fibroblast 3T3 cells (ATCC CRL-1658) were seeded at a density of 2×10^5 cells/mL in a 96-well plate. They were cultured overnight in DMEM medium supplemented with 10% FBS and penicillin/streptomycin (100 units/mL). The cells were maintained under 5% CO_2 at 37°C²⁹. Following a 24-h incubation period, the existing media were replaced. The cells were then exposed to different concentrations of the test compounds. Subsequently, they underwent an additional 24 h incubation. After this incubation period, the cells were washed. The MTT solution was added to the plate and incubated for 4 h. After incubation, dimethyl sulfoxide (100 μL) was added. This addition was maintained for 15 min at room temperature to dissolve formazan crystals. Subsequently, the absorbance at 540 nm was recorded using a microplate reader (BioTEK, USA)²⁴. The IC_{50} , representing the drug concentration (μM) causing cytotoxicity in 50% of the cells, was calculated accordingly.

DprE1 redox indicator assay

A redox indicator assay was conducted following a previously described protocol, utilising the reduction of resazurin to its fluorescent form, resorufin. In this assay, the DprE1 cofactor FAD undergoes reduction to FADH_2 , while the C-2 hydroxyl group of the substrate GGPR is oxidised to form a keto-intermediate known as geranylgeranylphosphoryl- β -d-2'-keto-erythro-penta-furanose (GGPX)^{11,40}. The inhibition of DprE1 was assessed using an activity assay, with the half maximal inhibitory concentration (IC_{50}) determined for each tested compound. Intermediate plates of compounds were prepared in V-bottomed 96-well plates, where the compounds were serially diluted twofold in DMSO. Subsequently, 1 μL of each compound dilution was pipetted in triplicate into Greiner black-bottomed 384 plates. The master mix (19 μL), comprising 5 μM DprE1, 50 mM Hepes pH 7.5, 100 mM NaCl, and 100 μM resazurin, was added to the compounds in the plate. The assay was initiated with 5 μL of 1 mM GGPR using the pump on the POLARstar Omega plate reader (BMG Labtech). Emission was measured at 590 nm with excitation at 530 nm at 37°C⁴¹. IC_{50} values were calculated using Prism GraphPad, fitting the data to a four-parameter dose–response curve. The initial rates of activity were used for the calculations, and fluorescence units were converted to μM resazurin reduced by referencing a resorufin standard curve.

Exploration of molecular interaction via molecular docking analysis

Utilising computational methods, docking serves as a valuable tool for investigating intermolecular interactions, with CDOCKER emerging as a prominent algorithm in this domain. CDOCKER employs a simulated annealing-based approach and relies on the CHARMM force field for structural representation^{24,42}. The three-dimensional (3D) X-ray crystal structure of the DprE1 protein (PDB ID: 4KW5) was initially obtained from the protein structure database (<http://www.rcsb.org>). The structure had a resolution of 2.61 Å. Subsequent to this, a protein preparation protocol was applied to rectify structural irregularities, including side chain corrections, loop region adjustments, and conformations. Meanwhile, ligands underwent processing to ensure correct chemical valences and charges. This step involved using the CHARMM all-atom force field²³.

Identification of the catalytic site for ligand binding on the target receptor was facilitated through a receptor cavity search. This search utilised the flood-filling algorithm and specifically focused on the DprE1 binding region, known as the catalytic site. Subsequently, the prepared receptor PDB and optimised ligand structure files underwent docking using the CDOCKER algorithm to unravel the molecular interactions. The potential binding site was identified with a volume of 1630.6 Å³ and a point count of 7066, using an equally spaced grid of 0.5 Å in the X, Y, and Z directions^{23,25}. The designed compounds were subjected to docking at a specified spherical site with coordinates 13.72 (X), -19.10 (Y), and 36.52 (Z). Conformations were randomly generated through 1000 dynamic steps with default simulation annealing. The interactions of the ligands in their docked poses were analysed, and subsequently, these interactions were considered for further MD simulations for a more in-depth examination.

Assessment of stability in protein–ligand complex using MD simulation

Through an MD simulation experiment, dynamic stability across a time span was verified for the static pose of the protein–ligand complex extracted from the molecular docking investigation. Further utilising energy graphs to visualise the relative stability, MD modelling was applied to natural protein structures in innate and docked complexes with ligands and pre-existing cofactor. To execute the simulations, GROMACS 2023 version on Ubuntu platform and other web-based servers were utilised⁴³. The protein and ligand topology files were constructed using the CHARMM27 force field. This process was conducted either externally via the SwissParam online server (<http://www.swissparam.ch/>) or internally using the native GROMACS platform. The innate and complex protein systems were virtually grouped in a triclinic box, with a distance cut-off of 1.0 nm separating the protein's outer surface from the box's edges and conserving Van der Waal interactions. The partial Mesh Ewald summation method, with a 1.0 nm cut-off, was utilised to compute coulombic interactions for long-range electrostatics. The system was explicitly solvated using the TIP3P water model, maintaining periodic boundary conditions. Next, the system's electro-neutrality was maintained by supplying the needed counter ions (Na⁺/Cl⁻)⁴⁴. Using the steepest descent algorithm, the whole system's energy was sequentially minimised over 5000 steps, with a tolerance of 1000 KJ mol⁻¹ nm⁻¹. Position constraints were applied to the complex to equilibrate the system. Canonical NVT and NPT ensembles were used to run 200 ps simulations at a constant temperature of 300 K and 1 bar of pressure. The initial velocities were generated following the Maxwell distribution. Temperature coupling was performed using velocity rescaling with a coupling constant of 0.1 ps. Temperature–pressure coupling was conducted using an extended ensemble Parrinello–Rahman algorithm, with a coupling constant of 2 ps. Consequently, a 300-ns MD production run with a 2-fs time step integration was applied to the equilibrated system. Every 500 steps, the trajectories were saved, the default GROMACS analytic tools were used for analysis, and the XMGRACE-5.1.22 program was used to visualise the data (<http://plasma-gate.weizmann.ac.il/Grace/>)^{29,45}.

Computational studies on ADMET and drug-likeness

Using the SwissADME web tool, various pharmacokinetic parameters for the top compounds were predicted. These include molecular weight (MW), TPSA, octanol-water partition coefficient (iLOGP), molecular refractivity (MR), aqueous solubility (ESOL LogS),

cytochrome-P450 enzyme inhibition, GI absorption, bioavailability score, skin permeation (Log Kp), Lipinsky violations, and PAINS alerts.

Acknowledgements

We thank Dr. Subhankar Mandal for helping in carrying out computational studies and MD simulation studies. The authors are thankful to the management of JSS Academy of Higher Education and Research, Mysore, for providing the necessary support.

Author contributions

Manisha Singh: conceptualisation, data gathering, statistical analysis, research, methodology development, verification, initial drafting, content refinement. Sarah M. Batt and Gurdyal S. Besra: biological experimental exploration, data collection, analytical scrutiny, manuscript refinement. Christian S.C. Canales and Fernando R. Pavan: biological experimental exploration, data collection, analytical scrutiny. Sethu Arun Kumar, Handattu S. Akshatha, and Meduri Bhagyalalitha: data compilation, analytical scrutiny, investigative efforts. Karthik G Pujar and Durgesh Bidye: data compilation, analytical scrutiny. Gurubasavaraj V. Pujar: idea conceptualisation, project management, supervision, initial drafting, manuscript enhancement.

Disclosure statement

The authors declare no conflicts of interest.

Funding

Funding has been awarded as follows: Personal Research Chair from Mr. James Bardrick, G.S.B. Medical Research Council MR/S000542/1, G.S.B. Medical Research Council MR/R001154/1, G.S.B. JSS Research Grant REG/DIR(R)/URG/54/2011–12/5293, M.S.

ORCID

Gurdyal S. Besra  <http://orcid.org/0000-0002-5605-0395>

Data availability statement

The authors confirm that the data supporting the findings of this study are available within the article [and/or] its [supplementary materials](#).

Appendix A. Supplementary data

[Supplementary data](#) to this article can be found within this manuscript.

References

- Zumla A, Chakaya J, Centis R, D'Ambrosio L, Mwaba P, Bates M, Kapata N, Nyirenda T, Chanda D, Mfinanga S, et al. Tuberculosis treatment and management—an update on treatment regimens, trials, new drugs, and adjunct therapies. *Lancet Respir Med.* 2015;3(3):220–234.
- Yuan T, Sampson NS. Hit generation in TB drug discovery: from genome to granuloma. *Chem Rev.* 2018;118(4):1887–1916.

3. Stojanovic Z, Gonçalves-Carvalho F, Marín A, Abad Capa J, Domínguez J, Latorre I, Lacoma A, Prat-Aymerich C. Advances in diagnostic tools for respiratory tract infections: from tuberculosis to COVID-19 – changing paradigms? *ERJ Open Res.* 2022;8(3):00113–2022.
4. Conradie F, Diacon AH, Ngubane N, Howell P, Everitt D, Crook AM, Mendel CM, Egizi E, Moreira J, Timm J, et al. Bedaquiline, pretomanid and linezolid for treatment of extensively drug resistant, intolerant or non-responsive multidrug resistant pulmonary tuberculosis. *N Engl J Med.* 2020;382(10):893–902.
5. Tiberi S, Utjesanovic N, Galvin J, Centis R, D'Ambrosio L, van den Boom M, Zumla A, Migliori GB. Drug resistant TB – latest developments in epidemiology, diagnostics and management. *Int J Infect Dis.* 2022; 124(Suppl 1):S20–S25.
6. Chikhale RV, Barmade MA, Murumkar PR, Yadav MR. Overview of the development of DprE1 inhibitors for combating the menace of tuberculosis. *J Med Chem.* 2018;61(19):8563–8593.
7. Hariguchi N, Chen X, Hayashi Y, Kawano Y, Fujiwara M, Matsuba M, Shimizu H, Ohba Y, Nakamura I, Kitamoto R, et al. OPC-167832, a novel carbostyryl derivative with potent antituberculosis activity as a DprE1 inhibitor. *Antimicrob Agents Chemother.* 2020;64(6):1–13.
8. Wang P, Batt SM, Wang B, Fu L, Qin R, Lu Y, Li G, Besra GS, Huang H. Discovery of novel thiophene-arylamide derivatives as DprE1 inhibitors with potent antimycobacterial activities. *J Med Chem.* 2021;64(9):6241–6261.
9. Finger V, Kucera T, Kafkova R, Muckova L, Dolezal R, Kubes J, Novak M, Prchal L, Lakatos L, Andrs M, et al. 2,6-Disubstituted 7-(naphthalen-2-ylmethyl)-7H-purines as a new class of potent antitubercular agents inhibiting DprE1. *Eur J Med Chem.* 2023;258:115611.
10. Yadav S, Soni A, Tanwar O, Bhadane R, Besra GS, Kawathekar N. DprE1 inhibitors: enduring aspirations for future antituberculosis drug discovery. *ChemMedChem.* 2023;18(16):e202300099.
11. Abrahams KA, Batt SM, Gurcha SS, Veerapen N, Bashiri G, Besra GS. DprE2 is a molecular target of the anti-tubercular nitroimidazole compounds pretomanid and delamanid. *Nat Commun.* 2023;14(1):3828.
12. Liu R, Lyu X, Batt SM, Hsu M, Harbut MB, Vilchêze C, Cheng B, Ajayi K, Yang B, Yang Y, et al. Determinants of the inhibition of DprE1 and CYP2C9 by antitubercular thiophenes. *Angewandte Chemie.* 2017;129(42):13191–13195.
13. Wang F, Sambandan D, Halder R, Wang J, Batt SM, Weinrick B, Ahmad I, Yang P, Zhang Y, Kim J, et al. Identification of a small molecule with activity against drug-resistant and persistent tuberculosis. *Proc Natl Acad Sci U S A.* 2013;110(27):E2510–E2517.
14. Kaushik CP, Chahal M. Synthesis and antibacterial activity of benzothiazole and benzoxazole-appended substituted 1,2,3-triazoles. *J Chem Sci.* 2020;132(1):1–10.
15. Kaushik CP, Pahwa A, Singh D, Kumar K, Luxmi R. Efficient synthesis, antitubercular and antimicrobial evaluation of 1,4-disubstituted 1,2,3-triazoles with amide functionality. *Monatsh Chem.* 2019;150(6):1127–1136.
16. Al-Blewi FF, Almeahmadi MA, Aouad MR, Bardaweel SK, Sahu PK, Messali M, Rezki N, El Ashry ESH. Design, synthesis, ADME prediction and pharmacological evaluation of novel benzimidazole-1,2,3-triazole-sulfonamide hybrids as antimicrobial and antiproliferative agents. *Chem Cent J.* 2018;12(1):1–14.
17. Kaushik CP, Sangwan J, Luxmi R, Kumar D, Kumar D, Das A, Kumar A, Singh D. Design, synthesis, anticancer and antioxidant activities of amide linked 1,4-disubstituted 1,2,3-triazoles. *J Mol Struct.* 2021;1226:1–13.
18. Kumar A, Lal K, Kumar V, Murtaza M, Jaglan S, Paul AK, Yadav S, Kumari K. Synthesis, antimicrobial, antibiofilm and computational studies of isatin-semicarbazone tethered 1,2,3-triazoles. *Bioorg Chem.* 2023;133:106388.
19. Faizan S, Prashantha Kumar BR, Lalitha Naishima N, Ashok T, Justin A, Vijay Kumar M, Bistuvalli Chandrashekarappa R, Manjunathaiah Raghavendra N, Kabadi P, Adhikary L, et al. Design, parallel synthesis of Biginelli 1,4-dihydropyrimidines using PTSA as a catalyst, evaluation of anticancer activity and structure activity relationships via 3D QSAR studies. *Bioorg Chem.* 2021;117:105462.
20. Mir F, Shafi S, Zaman MS, Kalia NP, Rajput VS, Mulakayala C, Mulakayala N, Khan IA, Alam MS. Sulfur rich 2-mercaptobenzothiazole and 1,2,3-triazole conjugates as novel antitubercular agents. *Eur J Med Chem.* 2014;76:274–283.
21. Madhura V, Revankar HM, Kulkarni MV. A new route for the synthesis of 4-arylacetamido-2-aminothiazoles and their biological evaluation. *Zeitschrift fur Naturforschung - B J Chem Sci.* 2015;70(7):483–489.
22. Ding X, Wu Y, Wang Y, Vilseck JZ, Brooks CL. Accelerated CDOCKER with GPUs, parallel simulated annealing, and fast Fourier transforms. *J Chem Theory Comput.* 2020;16(6):3910–3919.
23. Gagnon JK, Law SM, Brooks CL. Flexible CDOCKER: development and application of a pseudo-explicit structure-based docking method within CHARMM. *J Comput Chem.* 2016; 37(8):753–762.
24. Mandal S, Kumar BRP, Alam MT, Tripathi PP, Channappa B. Novel imidazole phenoxyacetic acids as inhibitors of USP30 for neuroprotection implication via the ubiquitin-Rho-110 fluorometric assay: design, synthesis, and in silico and biochemical assays. *ACS Chem Neurosci.* 2022;13(9):1433–1445.
25. Wu G, Robertson DH, Brooks CL 3rd, Vieth M. Detailed analysis of grid-based molecular docking: a case study of CDOCKER-a CHARMM-based MD docking algorithm. *2003;24(13):1549–1562.*
26. Mandal S, Chiriki DS, Gurupadayya BM, Chethan IA, Prashantha Kumar BR. Phenyl glycine incorporated glitazones as promising novel antidiabetic agents through PPAR γ agonism: design, synthesis and preclinical studies. *Eur J Med Chem Rep.* 2022;6:100067.
27. Van Der Spoel D, Lindahl E, Hess B, Groenhof G, Mark AE, Berendsen HJC. GROMACS: fast, flexible, and free. *J Comput Chem.* 2005;26(16):1701–1718.
28. Xie H, Li Y, Yu F, Xie X, Qiu K, Fu J. An investigation of molecular docking and molecular dynamic simulation on imidazopyridines as B-raf kinase inhibitors. *Int J Mol Sci.* 2015;16(11):27350–27361.
29. Mandal SP, Garg A, Prabitha P, Wadhvani AD, Adhikary L, Kumar BRP. Novel glitazones as PPAR γ agonists: molecular design, synthesis, glucose uptake activity and 3D QSAR studies. *Chem Cent J.* 2018;12(1):141.
30. Mandal SP, Reji A, Bhavimani G, Prabitha P, Durai P, Yuvaraj S, Shashank A, Krishna KL, Kumar BRP. Rational design, synthesis and evaluation of novel rodanine derivatives for antihyperglycemic activity. *Polycycl Aromat Compd.* 2022;42(4):1794–1805.
31. Lee J, Cheng X, Swails JM, Yeom MS, Eastman PK, Lemkul JA, Wei S, Buckner J, Jeong JC, Qi Y, et al. CHARMM-GUI input generator for NAMD, GROMACS, AMBER, OpenMM, and CHARMM/OpenMM simulations using the CHARMM36 additive force field. *J Chem Theory Comput.* 2016;12(1):405–413.
32. Piton J, Foo CSY, Cole ST. Structural studies of *Mycobacterium tuberculosis* DprE1 interacting with its inhibitors. *Drug Discov Today.* 2017;22(3):526–533.

33. Elumalai K, Elumalai M, Eluri K, Srinivasan S, Ashraf Ali M, Venkateswara Reddy B, Sarangi SP. Facile synthesis, spectral characterization, antimicrobial and in vitro cytotoxicity of novel N3,N5-diisonicotinyl-2,6-dimethyl-4-phenyl-1,4-dihydropyridine-3,5-dicarbohydrazide derivatives. *Bull Fac Pharm Cairo Univ.* 2016;54(1):77–86.
34. Ester. Synthesis and Biological Activity of Novel 1-(2,3,4-Trimethoxyphenyl)-2-[[5-(3,4,5-trimethoxyphenyl)-1,3,4-thiadiazol-2-yl]thio]ethanone Oxime. Vol. 43, Key Lab. Green Pestic. Agric. Biol. Eng., Res. Dev. Cent. Fine Chem., Guizhou Univ. 2006.
35. Mishra CB, Kumari S, Angeli A, Bua S, Tiwari M, Supuran CT. Discovery of benzenesulfonamide derivatives as carbonic anhydrase inhibitors with effective anticonvulsant action: design, synthesis, and pharmacological evaluation. *J Med Chem.* 2018;61(7):3151–3165.
36. Jivani AJ, Lunagariya KS, Kapadiya KM, Dholaria PV, Khedkar VM, Khunt RC. A step-by-step synthesis of S-methylene linker containing triazole-benzoxazole hybrids by click chemistry approach: anticancer activity in human cells. *Anal Chem Lett.* 2022;12(1):44–57.
37. Buchanan D, Pham AM, Singh SK, Panda SS. Molecular hybridization of alkaloids using 1,2,3-triazole-based click chemistry. *Molecules.* 2023;28(22):1–19.
38. Silva RTC, Guidotti-Takeuchi M, Peixoto JLM, Demarqui FM, Mori AP, Dumont CF, Ferreira GRA, Pereira GdM, Rossi DA, Corbi PP, et al. New palladium (II) complexes containing methyl gallate and octyl gallate: effect against *Mycobacterium tuberculosis* and *Campylobacter jejuni*. *Molecules.* 2023;28(9):3887.
39. Scarim CB, Pavan FR. Thiazole, triazole, thio- and semicarbazone derivatives - promising moieties for drug development for the treatment of tuberculosis. *Eur J Med Chem Rep.* 2021;1:100002.
40. Batt SM, Jabeen T, Bhowruth V, Quill L, Lund PA, Eggeling L, Alderwick LJ, Fütterer K, Besra GS. Structural basis of inhibition of *Mycobacterium tuberculosis* DprE1 by benzothiazinone inhibitors. *Proc Natl Acad Sci U S A.* 2012;109(28):11354–11359.
41. Batt SM, Toth S, Rodriguez B, Abrahams KA, Veerapen N, Chiodarelli G, Cox LR, Moynihan PJ, Lelievre J, Fütterer K, et al. Assay development and inhibition of the Mt-DprE2 essential reductase from *Mycobacterium tuberculosis*. *Microbiology (United Kingdom).* 2023;169(1):1–13.
42. Imran M, Abida Alotaibi NM, Thabet HK, Alruwaili JA, Asdaq SMB, Eltaib L, Kamal M, Alshammari ABH, Alshammari AMA, et al. Computer-assisted discovery of safe and effective DprE1/aaRSs inhibitors against TB utilizing drug repurposing approach. *J Infect Public Health.* 2023;16(4):554–572.
43. Hess B, Kutzner C, Van Der Spoel D, Lindahl E. GRGMACS 4: algorithms for highly efficient, load-balanced, and scalable molecular simulation. *J Chem Theory Comput.* 2008; 4(3):435–447.
44. Mark P, Nilsson L. Structure and dynamics of the TIP3P, SPC, and SPC/E water models at 298 K. *J Phys Chem A.* 2001;105(43):9954–9960.
45. Wang T, Brudvig GW, Batista VS. Study of proton coupled electron transfer in a biomimetic dimanganese water oxidation catalyst with terminal water ligands. *J Chem Theory Comput.* 2010;6(8):2395–2401.